

# **Do Saharan dust outbreaks affect weather forecast skill in Europe?**

Master's Thesis in Meteorology  
by

**Kilian Franz Hermes**

February 2022



INSTITUTE OF METEOROLOGY AND CLIMATE RESEARCH  
KARLSRUHE INSTITUTE OF TECHNOLOGY (KIT)

Supervisor:

Jun.-Prof. Dr. Christian Grams

Co-supervisor:

Prof. Dr. Corinna Hoose



*This document is licenced under the Creative Commons  
Attribution-ShareAlike 4.0 International Licence.*

---

## Abstract

Mineral dust is a prominent aerosol in the atmosphere. Dust aerosol directly interacts with radiation, altering the radiative budget and temperature structure in the atmosphere. Dust aerosol also affects clouds by acting as cloud condensation nuclei and ice nucleating particles. Models currently deployed for operational weather forecasting simplify dust by using climatologies for representing dust concentrations, hence misrepresenting dust effects during conditions which differ greatly from the climatology. Outbreaks of Saharan dust towards Europe occur several times a year and lead to elevated mineral dust concentrations over Europe. Such dust events often coincide with errors in operational weather forecasts.

In this thesis we systematically investigate errors in model analysis and short term forecasts during events of Saharan dust over Central Europe. We perform a case study for a dust event in spring 2021 and investigate the cause of model errors. For this we assess models which are currently used for operational weather forecasting as well as models with prognostic calculation of dust, and compare model analysis and forecast data with the observations from satellite and in-situ measurements. Furthermore, we construct an event catalog with 38 dust days between 2018 and mid 2021 and analyze the typical synoptic situation leading to dust events over Central Europe. We subsequently quantify the median model errors in cloudiness and surface radiation from a model used for operational weather forecasting by comparison against satellite products. For this we use brightness temperature as proxy for cloudiness and surface radiation as a measure for error propagation into further meteorological quantities.

We find misrepresentation of mineral dust the source of model errors during the event in spring 2021. The inclusion of prognostic aerosol and direct radiative effects from dust improves the forecast in surface radiation during clear-sky conditions, but is not sufficient for reproducing cloudiness during the dust events. We find two typical synoptic situations leading to Saharan dust over central Europe. Most frequently, an omega situation with the high pressure center over Central Europe, and a situation with a trough over the Iberian peninsula, northwest Africa, and a weakly pronounced ridge over Central Europe. We find weak indications for a longer transport path of dust towards Central Europe for the former, and a more direct transport for the latter synoptic situation. For dust days in the event catalog we find a significant overestimation of brightness temperature (underestimation of dust direct radiative effects, cloud top height, cloud optical depth) for cases with dust compared to cases without dust. For surface radiation we find a median overestimation of about 15% during cloudy conditions with dust compared to cloudy conditions without dust. For clear-sky conditions we do not find reliable differences, as the satellite retrieval is biased during such conditions.

Our findings show that the models deployed for operational weather forecasting do not adequately reproduce cloudiness during events with Saharan dust over Central Europe. The missing implementation of prognostic dust, in particular indirect effects on cloud formation, still leads to significant underestimations of cloudiness and overestimations of surface radiation during dust events. Our study therefore highlights the need of including such effects into future forecast systems.



---

## Zusammenfassung

Mineralstaub ist ein wichtiges und weit verbreitetes Aerosol in der Atmosphäre. Staubaerosol beeinflusst direkt den Strahlungshaushalt und ist weiterhin effektiv als Kondensationskeim und Eiskeim und beeinflusst damit Wolkeneigenschaften. Derzeit für die operationelle Wettervorhersage eingesetzte Modelle vereinfachen Staubprozesse und nutzen klimatologische Mittelwerte für die Implementierung von Staubkonzentration. Dies führt zur fehlerhaften Abbildung von Staubprozessen, insbesondere in Situationen mit überdurchschnittlichen Konzentrationen von Mineralstaub.

Ereignisse mit dem Transport großer Mengen Saharastaub nach Europa treten mehrmals im Jahr auf und führen zu stark überdurchschnittlichen Konzentrationen von Mineralstaub über Europa. Solche Staubereignisse fallen oft mit Fehlern in der operationellen Wettervorhersage zusammen. In dieser Arbeit untersuchen wir Fehler in Modellanalysen und Kurzfristprognosen während Saharastaubereignissen über Mitteleuropa. In einer Fallstudie analysieren wir ein ausgewähltes Staubereignis des Frühjahrs 2021 und untersuchen die Ursachen der Modellfehler. Hierzu nutzen wir Modelle, welche derzeit für die operationelle Wettervorhersage eingesetzt werden sowie Modelle mit prognostischer Berechnung von Staub. Für die Analyse von Fehlern vergleichen wir Modellanalysen und Vorhersagedaten mit Daten von Satelliten und in-situ Messungen. Aufbauend auf der Fallstudie definieren wir einen Ereigniskatalog über 38 Staubtage von 2018 bis Mitte 2021. Anhand des Ereigniskatalogs untersuchen wir typische Wetterlagen, welche zu Staubereignissen über Mitteleuropa führen. Anschließend quantifizieren wir die Modellfehler in Bewölkung und solarer Einstrahlung für ein in der operationellen Wettervorhersage verwendetes Modell. Hierfür vergleichen wir Modelldaten mit Satellitenprodukten und verwenden die Strahlungstemperatur als Proxy für hohe Bewölkung und solare Einstrahlung als Maß für die Fehlerfortpflanzung in weitere meteorologische Größen.

Wir kommen zu dem Ergebnis, dass Mineralstaub die Ursache für Modellfehler während des Ereignisses im Frühjahr 2021 ist. Die Implementierung von prognostischem Aerosol und direkten Strahlungseffekten von Staub verbessert die Vorhersage solarer Einstrahlung bei wolkenfreiem Himmel, reicht aber nicht aus, um Bewölkung während Staubereignissen zu reproduzieren. Wir finden zwei typische Wetterlagen, welche zu Saharastaub über Mitteleuropa führen. Die häufigste ist eine Omegalage mit Hochdruckzentrum über Mitteleuropa. Es folgt eine Wetterlage mit Trog über der Iberischen Halbinsel und Nordwestafrika und einem nur schwach ausgeprägten Rücken über Mitteleuropa. Außerdem deuten sich ein längerer Transportweg des Staubes nach Mitteleuropa für die Omegalage und ein direkterer Transportweg für die Lage mit Trog und schwachem Rücken an. Für die Staubtage des Ereigniskatalogs finden wir eine signifikante Überschätzung der Strahlungstemperatur (d.h. Unterschätzung des direkten Strahlungseffekts von Staubs, der Wolkenobergrenze oder der optischen Dicke der Wolken) für Bedingungen mit Staub im Vergleich zu Bedingungen ohne Staub. Für solare Einstrahlung finden wir eine mittlere Überschätzung von etwa 15% während Bewölkung mit Staub im Vergleich zu Bewölkung ohne Staub. Für wolkenfreie Bedingungen können wir keine eindeutigen Unterschiede finden, da das Satellitenprodukt unter solchen Bedingungen einen systematischen Fehler aufweist.

---

Unsere Ergebnisse zeigen, dass auch Modelle, welche im Jahr 2021 für die operationelle Wettervorhersage eingesetzt werden, die Bewölkung während Staubereignissen über Mitteleuropa nicht adäquat reproduzieren. Die fehlende prognostische Berechnung von Staub, insbesondere von indirekten Effekten auf Wolkenbildungsprozesse, führt immer noch zu einer signifikanten Unterschätzung der Bewölkung und Überschätzung der solaren Einstrahlung. Unsere Studie unterstreicht daher die Notwendigkeit, solche Effekte in zukünftige Modellversionen einzubeziehen.

# Contents

<b>1</b>	<b>Introduction</b>	<b>1</b>
<b>2</b>	<b>Background Information</b>	<b>3</b>
2.1	Dust in the Atmosphere . . . . .	3
2.2	Aerosol Effects on Meteorological and Radiative Quantities . . . . .	3
2.3	Aerosol Processes and Interactions in NWP Models . . . . .	4
<b>3</b>	<b>Data and Methodology</b>	<b>7</b>
3.1	Model Derived Data . . . . .	7
3.1.1	ECMWF IFS . . . . .	7
3.1.2	Copernicus Atmosphere Monitoring Service . . . . .	8
3.1.3	ICON-ART . . . . .	8
3.1.4	ERA5 Reanalysis . . . . .	9
3.2	Measurement Data . . . . .	9
3.2.1	Meteosat-based Cloud and Radiation Products . . . . .	9
3.2.2	GridSat Cloud Top Products . . . . .	11
3.2.3	CALIPSO-CALIOP Aerosol Products . . . . .	11
3.2.4	Aeronet Measurement Network . . . . .	12
3.3	K-means Clustering . . . . .	13
3.4	Bootstrapping and Difference of Medians . . . . .	13
3.5	Brightness Temperature from Model Variables . . . . .	13
<b>4</b>	<b>Event Selection and Data Verification</b>	<b>15</b>
4.1	Events in Spring 2021 and Selection for Case Study . . . . .	15
4.2	Event Catalog and Selection Criteria . . . . .	16
4.3	Validation of CAMS Dust Data . . . . .	18
<b>5</b>	<b>Case Study: Dust Outbreak on 03 March 2021</b>	<b>21</b>
5.1	Synoptic Overview . . . . .	23
5.2	Dust Transport towards Central Europe . . . . .	25
5.3	Comparison to Satellite Data . . . . .	32
5.4	Comparison to Radiosonde Data . . . . .	36
5.5	Comparison to Station Data . . . . .	38
5.6	Summary of Case Study . . . . .	41

<b>6</b>	<b>Generalization: Dust Outbreak Synoptics and Forecasting Errors</b>	<b>43</b>
6.1	Synoptic Analysis . . . . .	44
6.1.1	General Synoptic Situation . . . . .	44
6.1.2	Seasonality of Dust Outbreaks . . . . .	46
6.1.3	Dust Emission Regions and Transport . . . . .	46
6.2	Quantitative Analysis . . . . .	48
6.2.1	Methodology and Case Classification . . . . .	48
6.2.2	Threshold Sensitivity Analysis . . . . .	49
6.2.3	Quantitative Results . . . . .	51
6.3	Cases with Inverse Cloudiness in Model and Satellite . . . . .	54
6.4	Summary of Generalization . . . . .	55
<b>7</b>	<b>Discussion and Conclusion</b>	<b>57</b>
	<b>Abbreviations</b>	<b>62</b>
	<b>Bibliography</b>	<b>68</b>

# 1 Introduction

Dust is the most common natural aerosol in Earth's atmosphere by mass (Textor et al., 2006) and interacts with various components of the Earth system (Carslaw et al., 2010). Like other aerosol species, mineral dust directly interacts with radiation, by scattering and absorbing solar radiation and absorbing and emitting terrestrial radiation (Liao and Seinfeld, 1998). As a consequence of this direct effect, the absorption of radiation by aerosol alters the temperature structure of the atmosphere. This is known as the semi-direct effect (Hansen et al., 1997). Mineral dust particles also interact with microphysical processes via acting as cloud condensation nuclei (CCN) or ice nucleating particles (INP) (Karydis et al., 2011). This alters cloud properties such as cloud brightness, cloud top height or cloud lifetime and can lead to generally increased cloudiness and is known as indirect effect (Lohmann and Feichter, 2005). Models which are currently used for numerical weather prediction (NWP) make simplifications with respect to dust to circumvent computational costs. On one hand, dust emission, transport and concentrations are not calculated prognostically. Instead, operational NWP models rely on climatological mean values (e.g. ECMWF 2021a, Reinert et al. 2021) for implementing dust effects. On the other hand, even in the models with prognostic calculation of dust life cycle, the direct, semi-direct and indirect effects of dust are only partially implemented (e.g. Flentje et al. 2021).

The Sahara is the dominant source of mineral dust on Earth (Shao et al., 2011). Mineral dust can be picked up by wind and transported over large distances, such as from the Sahara to Europe. Consequentially, the Mediterranean and Europe are frequently affected by outbreaks of Saharan dust (e.g. d'Almeida 1986, Moulin et al. 1998). Previous studies assess whether the inclusion of dust effects on clouds into models leads to improvements of forecasts during dust events in Europe. Weger et al. (2018) find that especially cirrus cloud cover and ice content increase with including prognostic calculation of dust and its effects. Rieger et al. (2017) assess the effect of dust on forecasts of photovoltaic (PV) power generation, a technology which is rapidly gaining importance in a world moving to sustainable forms of energy supply. The forecast of PV power generation relies on the forecast of global radiation, and shortcomings in the NWP models especially in cloudiness can cause large errors (Köhler et al., 2017). Rieger et al. (2017) find an improvement of radiation forecast by including prognostic calculation of dust and its effects, where the direct radiative effect from dust dominates the improvements.

During spring 2021, several outbreaks of Saharan dust with dust transport towards Europe occurred, leading to elevated dust concentrations (highly above average) over Germany for several days. During these days, also the PV forecast for parts of Germany shows large overestimations (figure 1.1), highlighting the continuing problem of forecast errors during such events. Recent investigation of a

selected dust event over the Iberian peninsula during spring 2021 shows misrepresentations in cirrus cloud cover, surface radiation and 2 m temperature in the forecast from the operational NWP model of the European Centre for Medium-Range Weather Forecasts (ECMWF), and improvements in forecasts with prognostic calculation of dust and the inclusion of dust radiative effects (Magnusson et al., 2021).

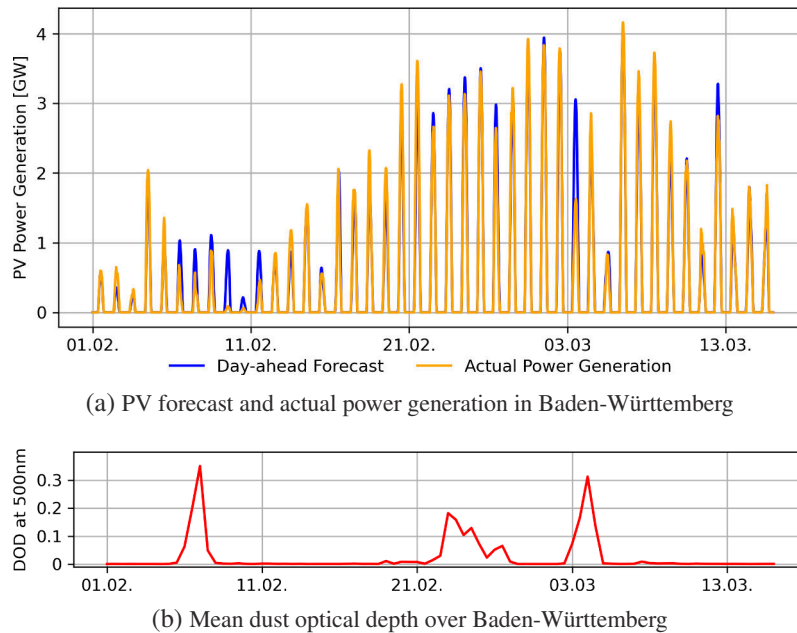


Figure 1.1: PV forecast, actual power generation and dust optical depth for Baden-Württemberg from February until mid March 2021. PV data from TransnetBW, operator of the electrical grid in Baden-Württemberg. Dust data from the Copernicus Atmosphere Monitoring Service.

This thesis project picks up this point and further investigates the effects of Saharan dust outbreaks towards Europe by addressing the following main research questions:

- What is the cause for the prominent model errors during the dust events in spring 2021?  
Is dust related to the model errors or are other processes or quantities causing the errors?
- What is the general synoptic situation leading to dust events over Central Europe?
- How can model errors during dust events be quantified? How large are the typical errors during dust events over Central Europe?

This thesis is organized as follows: Chapter 2 gives an overview about mineral dust, effects on radiation and implementation of this in current models. Chapter 3 gives an overview about the data products which are used for this thesis and summarizes model implementations or retrieval methods for the data products. Chapter 4 outlines the criteria by which the analyzed events were selected and validates dust model data for these events. Results are then structured in two chapters: Chapter 5 presents results from the case study of a specific event in spring 2021 and aims to trace back model errors to its cause. Chapter 6 picks up on the findings from the case study and seeks to generalize the typical synoptic situation of dust outbreaks towards Central Europe and to quantify model errors. Finally chapter 7 summarizes our results and draws conclusions with an outlook on future research.

## 2 Background Information

For understanding the context of this thesis, it is necessary to have an overview about the role of mineral dust in the atmosphere and how this is represented in models. This chapter first provides a brief and general overview about mineral dust in the Earth system and atmosphere. Subsequently, it summarizes key effects of aerosol, and mineral dust in particular, on radiation and cloud variables. Finally we discuss the implementation of aerosol processes in state-of-the-art NWP models and outline shortcomings of current implementations.

### 2.1 Dust in the Atmosphere

Mineral dust is the most common aerosol in Earth's atmosphere by mass (Textor et al., 2006). Estimates for global mineral dust emissions range from 1000 to 5000 Tg yr<sup>-1</sup>, with the largest sources being the north African desert regions, East and Central Asian deserts and plains and the Australian desert regions (Shao et al., 2011). The properties of mineral dust are not uniform but depend on the chemical composition and mineralogy of particles, which often can be linked to the source region (Muhs et al., 2014). Once emitted into the atmosphere, mineral dust can be transported over large distances (d'Almeida 1986, Moulin et al. 1998). During its residence time in the atmosphere, mineral dust is exposed to various chemical and microphysical processes, which can alter its properties (Baker et al., 2014).

### 2.2 Aerosol Effects on Meteorological and Radiative Quantities

Aerosol particles in the atmosphere affect weather and climate via various processes, which can be summarized as follows: First, aerosol particles directly interact with radiation, by scattering and absorbing solar radiation and by scattering, absorbing and emitting terrestrial radiation. This is known as the direct aerosol effect (see Haywood and Boucher 2000 for a review). Second, absorption of radiation via the direct aerosol effect leads to a heating of the surrounding air and hence alters the temperature profile. This can also result in the evaporation of cloud droplets and is known as the semi-direct aerosol effect (Hansen et al., 1997). Third, aerosol particles act as cloud condensation nuclei (CCN) and ice nucleating particles (INP), altering various cloud properties. This is known as the indirect aerosol effect (see Lohmann and Feichter 2005 for a review).

Indirect aerosol effects include a variety of processes. Increased availability of CCN and INP in

clouds with fixed water amounts reduces cloud droplet size and increases the cloud droplet number concentration (CDNC). An increased CDNC at constant (or enhanced) cloud moisture leads to an enhanced cloud reflectivity via an increased back scattering cross section (Twomey, 1974). A reduced cloud droplet size reduces the precipitation efficiency (Rosenfeld, 2000) and can lead to extended cloud lifetime (Albrecht, 1989). Based on the modification of cloud properties and precipitation formation processes, several further indirect effects are suggested in literature, i.e. faster or delayed glaciation of clouds, increased precipitation formation via the ice phase (Lohmann and Feichter, 2005).

For the effects of mineral dust in particular, already early lab studies observed high ice nucleation abilities (e.g. Isono et al. 1959). Field experiments find Saharan mineral dust particles to be effective INP for glaciating mildly supercooled altostratus clouds (Sassen et al., 2003), while lab studies from the same campaign confirm the high effectiveness of mineral dust for ice nucleation (DeMott et al., 2003). More recent studies performing in-situ sampling of cirrus crystals and analyzing residual particles after ice sublimation found mineral dust and metallic particles to be the dominant particle in cirrus ice crystals and heterogeneous freezing being the dominant freezing mechanism (Cziczo et al., 2013).

In summary, atmospheric aerosol and mineral dust in particular, interacts with radiation and the climate system via various processes. Firstly, via direct interaction with radiation, and semi-directly via altering the temperature profile in the atmosphere. Secondly, via altering cloud properties which indirectly modifies radiation quantities. Via these processes, aerosol has a considerable effect on the radiative budget. It is therefore essential to understand the effects of mineral dust in order to advance with understanding of weather and climate as a whole.

### 2.3 Aerosol Processes and Interactions in NWP Models

As explained above, aerosol effects (direct, semi-direct and indirect) have a considerable impact on the radiative budget of the Earth system. It has long been recognized that inclusion of aerosol processes and interactions is essential for climate projection purposes (Boucher et al., 2013). However, including online calculation of aerosol and chemical processes in NWP models has become popular only recently. Simulating these processes requires fully-coupled models for meteorological, chemical, physical, and biological processes and comes at the expense of high computational demands (Zhang, 2008).

The development of such coupled models, which dynamically take into account feedbacks between meteorological, chemical and physical processes has evolved rapidly in recent years. Today, advanced approaches for representing aerosol size distributions via bins, modes (Zhang et al., 1999) or modal distributions (Ackermann et al., 1998) are available, which is used in more recent model developments (Zhang, 2008). Current models prognostically calculate aerosol emissions, transport, removal and interaction processes (e.g. Rieger et al. 2015) and confirm the vital role of prognostic aerosol modeling in prediction of cloudiness and radiation (Rieger et al. 2017, Weger et al. 2018, Magnusson et al. 2021).

In contrast, many models currently deployed for operational weather forecasting use prescribed monthly or seasonal climatologies for aerosol and trace gases (e.g. Reinert et al. 2021, ECMWF 2021a) to circumvent high computational costs. Figure 2.1 shows a seasonal climatology of dust, based on the same data as the monthly climatology used for the operational version of ECMWF IFS (Bozzo et al., 2017), and a dust analysis from the near-real-time forecast from the CAMS model, which extends the ECMWF IFS with aerosol processes (Rémy et al., 2019). Climatology and analysis roughly agree in patterns of elevated dust concentrations, indicating consistency between climatology and near-real-time analysis concerning regions which typically show elevated dust concentrations. Individual events with above average concentrations however are not captured with the prescribed climatology. Peak values in the CAMS dust analysis over North Africa and Europe, which shows an event of Saharan dust outbreak towards Europe, are not visible in the climatology.

Previous studies have examined improvements in model prediction skill with increasing the complexity of aerosol implementations in operational NWP models. Morcrette et al. (2011) used the ECMWF IFS model extended for aerosol, cloud, radiation interactions and find considerable differences of the model simulated aerosol distributions compared to the climatologies used in the operational model version, however no clear improvements of fully interactive aerosol compared to analyzed and then fixed aerosol. Mulcahy et al. (2014) use the Met Office Unified Model, finding improvements of in aerosol optical depth and a reduction in temperature bias due to direct aerosol effects. Inclusion of indirect aerosol effects however improves the forecast in some areas only.

In summary, current NWP models used for operational forecasting simplify dust processes due to the implementation of aerosol via prescribed climatologies. This can lead to forecast errors, some of which can be reduced with increasing the complexity of aerosol implementations.

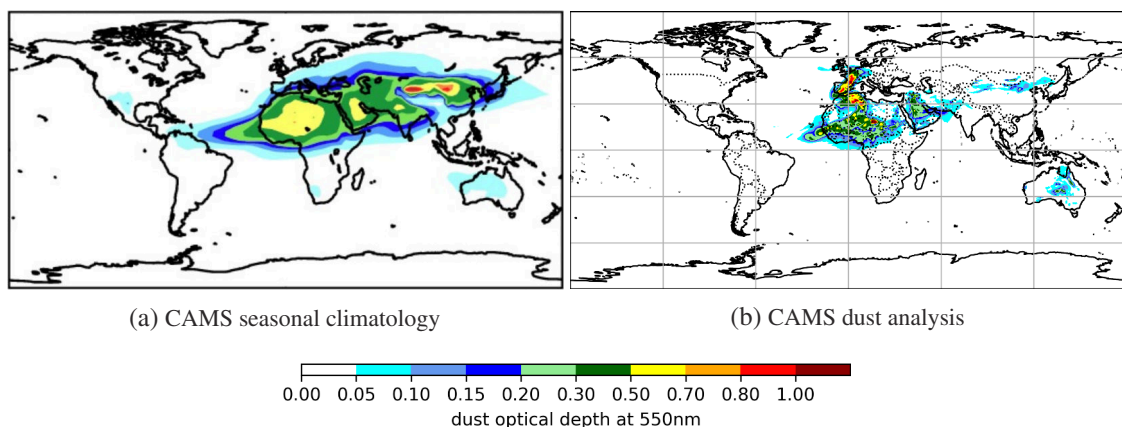


Figure 2.1: Global dust climatology from CAMS model for the months March–May (figure from ECMWF 2020b, after Bozzo et al. 2017) and global aerosol near-real-time analysis from CAMS model for 03 March 2021, 00 UTC.



## 3 Data and Methodology

For this thesis we use a variety of model and measurement data. This chapter gives a brief overview about model specifications, data retrieval algorithms as well as limitations and shortcomings for the different data sources and retrieval methods. The last part of this chapter summarizes key methods which are used for analysis.

### 3.1 Model Derived Data

For assessing forecast skill and errors during dust events, the central research question of this thesis, we use data from two model families. Firstly from the Integrated Forecasting System (IFS) developed by the European Centre for Medium-Range Weather Forecasts (ECMWF), and secondly from the ICON model which is currently deployed by the German weather service (DWD). The following gives a brief summary about model characteristics and implementations of aerosol effects.

#### 3.1.1 ECMWF IFS

For analysis of forecast quality, we use analysis and forecast data from the IFS, a general circulation model (GCM) model which is developed by the ECMWF. We use data from the most recent operational version at each date, namely from the versions CY43R3 to CY47R1. The IFS provides two forecasts from unperturbed initial conditions. A forecast at the regular horizontal model resolution of 18 km (ECMWF, 2020a), and a forecast with an increased horizontal resolution of 9 km (hres) (ECMWF, 2021b). Additionally a medium-range ensemble forecast (ENS) is provided, containing 50 model runs from perturbed initial conditions which are generated by adding small amplitude perturbations, and stochastically perturbed model physics during the model integration. All simulations are performed with 137 vertical levels, spanning from surface pressure to 0.01 hPa at the top level. Model initialization is performed at 00 and 12 UTC (ECMWF, 2020a). For the purpose of this thesis we retrieve Total Cloud Cover (TCC) and Surface Incoming Shortwave Radiation (SIS) from the ENS, and simulated brightness temperature (BT) from the hres run, both with 0.25° grid spacing. For analysis we only consider forecast lead times of less than 12 hours. The IFS uses prognostic variables for temperature, humidity, cloud properties as well as monthly-mean climatologies of trace gases and aerosols as input for radiative calculations. The aerosol climatologies are derived from analysis and short-time forecast data within the Copernicus Atmosphere Monitoring Service (CAMS) (Bozzo et al., 2017). The Rapid Radiation Transfer Model deployed in IFS takes cloud-radiation interactions into account (ECMWF, 2020b).

### 3.1.2 Copernicus Atmosphere Monitoring Service

For identifying dust events and assessing dust transport, we use near-real-time forecast data from the IFS-AER model. The IFS-AER is developed within the CAMS framework and provides the operational IFS model with extensions for simulating tropospheric aerosols, chemically interactive gases, and greenhouse gases. The horizontal model resolution is 40 km with 60 (137 after 9 July 2019) vertical levels, spanning from surface pressure to 0.01 hPa at the top level. Model initialization is performed at 00, 06, 12 and 18 UTC (Rémy et al., 2019). For the purpose of this thesis we retrieve DOD data with 0.25° grid spacing, from the time of model initialization (analysis).

Dust emissions in IFS-AER are computed dynamically using prognostic variables from the meteorological model, emission threshold speeds are derived from a climatology. A bulk-bin aerosol scheme is used for modeling aerosol size distributions. For mineral dust this is three bins within the limits 0.03, 0.55, 0.9, 20  $\mu\text{m}$  which represent the fine, coarse and super-coarse mode. Since IFS cycle 45R1 (26 June 2018), operational reanalysis and forecast is performed with interactive aerosols as input for the radiative scheme, hence includes direct aerosol radiative effects into the computation. Currently there is no representation of aerosol-cloud interactions in IFS-AER, however an implementation is planned for the future (Rémy et al., 2019).

Studies have evaluated aerosol forecast from IFS-AER with ceilometer measurement data, concluding realistic representation of Saharan dust on spatiotemporal scales  $>100$  km and  $> 0.5$  d, however with a light overestimation during most days (Flentje et al., 2021).

Due to its shared code base with the ECMWF IFS, which we use for analysis of model errors, good representation of dust transport, and free data availability, we use data from IFS-AER as a first diagnostic to assess dust transport and spatial distribution. Hereafter we refer to the IFS-AER as *CAMS model*.

### 3.1.3 ICON-ART

For an in-depth study, we use data from the ICON-ART model. ICON-ART is based on the ICOSahedral Nonhydrostatic weather and climate model (ICON), jointly developed by DWD and the Max Planck Institute for Meteorology. ICON is a non-hydrostatic GCM and was developed with the aim of providing a global model for both weather and climate predictions. It is based on an icosahedral grid and allows local grid refinement, so called nesting (Zängl et al., 2015). The ICON model is used for operational weather forecasting by the DWD on global scale since January 2015 and on regional scale since 2016 (Reinert et al., 2021).

ART (Aerosol and Reactive Trace gases) is submodule of ICON developed at Karlsruhe Institute of Technology, which enables the life cycle of aerosol, trace gases and their interactions the atmosphere. In ICON-ART, aerosol processes are simulated online, including emission and removal processes. Aerosol particles are represented by log-normal modes, where the median diameter of the distribution is a diagnostic variable (Rieger et al., 2015). ICON-ART is under ongoing development (Schröter et al., 2018) and includes tropospheric and stratospheric chemistry, aerosol chemistry, aerosol dynamics and impact of gases and aerosols on radiation and clouds (Rieger et al., 2015). At the time of this thesis project, only direct interactions of aerosol with radiation was

implemented into the here used pre-operational version. Aerosol cloud interactions were not yet implemented into the operational version. All data from ICON-ART which we use in this thesis was calculated on a R2B06 global domain with R2B07 nest over north Africa and Europe with 60 vertical levels, which translates to an effective horizontal resolution of 19.7 km. The model was initialized at 00 UTC. We retrieve DOD, SIS and variables for the calculation of simulated BT (pressure, temperature, specific humidity, cloud water mixing ratio, cloud ice mixing ratio) on the native icosahedral grid. For analysis we only consider forecast lead times of less than 24 hours.

### 3.1.4 ERA5 Reanalysis

For synoptic analysis, we use ERA5 reanalysis data provided by ECMWF (Hersbach et al., 2020). Model reanalysis was introduced for providing a consistent set of atmospheric analysis products, via combining the record of past atmospheric observations with a fixed, state-of-the-art data assimilation system (Trenberth and Olson, 1988). Today, reanalysis is widely applied in research, i.e. for studying changing climate or improvements in modeling and assimilation capabilities or to obtain state-of-the-art climatologies. ERA5 is the most recent global reanalysis product from ECMWF and covers the period from 1950 to present. It replaces its predecessor ERA-Interim and is continuously extended to include most recent dates. ERA5 reanalysis is calculated with the ECMWF IFS model in version 41r2. The horizontal resolution is 31 km with 137 vertical levels, spanning from surface pressure to 0.01 hPa at the top level (Hersbach et al., 2020) For the purpose of this thesis we retrieve pressure and geopotential height with 0.25° grid spacing.

## 3.2 Measurement Data

For the validation of model data and as reference for the calculation of model errors, we use measurement data from satellite based instruments as well as station data. The following gives a brief summary about algorithms and methods used for retrieving satellite products.

### 3.2.1 Meteosat-based Cloud and Radiation Products

We use datasets for cloud mask and Surface Incoming Shortwave Radiation (SIS), derived from measurements with the Spinning Enhanced Visible and Infrared Instrument (SEVIRI). SEVIRI instruments are the main instruments based on the geostationary Meteosat Second Generation (MSG) satellites. SEVIRI employs twelve spectral channels, spanning from the visible range to infrared (0.4 - 13.4  $\mu\text{m}$ ). It provides a sampling resolution of 1 to 3 km at nadir, and is continuously scanning with a 15 min repeat cycle (Aminou, 2002).

## **Meteosat Cloud Mask**

We use the MSG cloud mask which is derived via the *scenes analysis* algorithm. Several products derived from the MSG image data require information about the type of scene contained within a pixel (some products are derived from cloudy pixels, others from clear pixels only). The scenes analysis algorithm identifies whether a pixel contains clouds or not. Pixels partially covered by clouds or covered with semi-transparent clouds are marked as cloudy pixels. Pixels identified as clear are assigned the information of the underlying surface type (land/sea), which is taken from a surface type map.

The retrieval algorithm is based on a threshold technique which compares the expected clear-sky radiance on several IR channels to the measured radiance per pixel. Specific thresholds are calculated for each pixel and zenith angle. Scenes are then identified based on the deviation of measured radiance from the calculated thresholds. The output from the scenes analysis algorithm is then used for creating a cloud mask, which contains the classes: clear sky over water, clear sky over land, cloud, no data (EUMETSAT 2015; for more information about the algorithm see Derrien and Le Gléau 2005). The MSG cloud mask covers a circular area with maximum extends of  $-67.5^{\circ}\text{S}$  to  $67.5^{\circ}\text{N}$  and  $-67.5^{\circ}\text{W}$  to  $67.5^{\circ}\text{E}$  on pixel basis and is saved on a space perspective grid (EUMETSAT, 2009).

## **Surface Incoming Shortwave Radiation**

We use SIS derived via SARAH-2 methods, which employ the MAGIC SOL method for the calculation of radiative variables. MAGIC SOL is based on the Heliosat procedure (Beyer et al., 1996) and uses reflection measurements from the visible channels (VIS006 and VIS008) to determine the effective cloud albedo. For the calculation of solar irradiance during cloudy conditions, the retrieved effective cloud albedo and a clear-sky model are used. No information from infrared channels is required. Additionally a climate algorithm is applied to account for technical changes between the SEVIRI instrument and its predecessor MVIRI, and in order to increase consistency with data derived from measurements with earlier instruments.

For the calculation of solar irradiance during clear-sky conditions, a look-up table approach is used which takes into account the effects from aerosol, water vapor and ozone. For aerosols, a modified monthly mean climatology derived from the ECMWF MACC (Monitoring Atmospheric Composition and Climate) project, a predecessor to the CAMS described in section 3.1.2, is used. For water vapor, the vertically integrated value is taken from the daily ECMWF high-resolution analysis at 12 UTC. For ozone, monthly mean values of the vertically integrated ozone column from ERA-Interim reanalysis are used (Pfeifroth and Trentmann, 2018).

For the purpose of this thesis, we use the current operational SIS product (Interim Climate Data Records) derived via the SARAH-2.0 method, product version 410. It is recorded from instruments on Meteosat-11 (EUMETSAT, 2021a) and covers a circular area with maximum extends of  $-65^{\circ}\text{S}$  to  $65^{\circ}\text{N}$  and  $-65^{\circ}\text{W}$  to  $65^{\circ}\text{E}$  with a resolution of 0.5 degree. This product is available for all dates from 2018-02-20 to present with the same version of retrieval algorithm (EUMETSAT, 2021b).

As this thesis examines events with high dust loads, the sensitivity of the applied method to aerosol

variations must be taken into account. For the here described method, deviations in aerosol optical depth (AOD) of 0.1 relative to a background of AOD of 0.2 lead to uncertainties in SIS of about  $10 \text{ W m}^{-2}$  for a solar zenith angle of 60 degree, and to uncertainties of about  $20 \text{ W m}^{-2}$  for a solar zenith angle of 0 degree, both under clear-sky conditions. For cloudy conditions, uncertainties are reduced significantly due to increased total optical depth from clouds (Pfeifroth and Trentmann, 2018). As the direct radiative effect of aerosol is implemented with a prescribed climatology, we expect the satellite product to overestimate SIS for cases with above average AOD.

### 3.2.2 GridSat Cloud Top Products

For accessing cloud top variables we use BT data from the GridSat satellite product. The GridSat product combines data from most international meteorological satellites in geostationary orbit and provides an intersatellite calibrated product, covering most of the globe between  $70^\circ\text{S}$  and  $70^\circ\text{N}$  from 1980 until present. It is continuously extended to include most recent dates. The spatial resolution is  $0.07^\circ$ , which is equivalent to about 8 km at the equator. The temporal resolution is 3 h. GridSat provides data in three channels (infrared, water vapor, visible) (Knapp et al., 2011). For the purpose of this thesis we use the *NOAA FCDR of Brightness Temperature near 11 microns* (irwin\_cdr) variable as a measure for cloud top temperature.

### 3.2.3 CALIPSO-CALIOP Aerosol Products

For assessing cloud and aerosol properties in vertical cross sections, we use data from the Cloud-Aerosol Lidar with Orthogonal Polarization (CALIOP) based on the Cloud-Aerosol Lidar and Infrared Pathfinder Satellite Observations (CALIPSO) satellite. CALIPSO is part of the A-train satellites which feature a 705 km sun-synchronous polar orbit with an inclination of  $98.28^\circ$ . These orbit properties enable a 16-day repeat cycle and a global coverage between  $82.8^\circ\text{N}$  and  $82.8^\circ\text{S}$ . CALIOP is equipped with two laser channels (1064 nm, 532 nm), both sending coaligned pulses. The 532 nm laser sends polarized pulses, the corresponding backscattered signal is detected with parallel and perpendicular polarization relative to the polarization of the emitted signal. The depolarization ratio and backscatter from both channels is then used for calculating a variety of cloud and aerosol products.

The retrieval of cloud and aerosol properties is based on the scene classification algorithms, which first classify the type (cloud, aerosol, clear-sky) of the layer. A layer is detected via a threshold approach, which tests enhancements of backscatter above the expected molecular backscatter. This works from the uppermost detected cloud or aerosol layer downwards, in order to correct retrievals from lower layers with information derived for the attenuation from overlying layers. If a layer is detected, the scene classification is performed, which uses a set of algorithms based on statistical differences in optical and physical properties of clouds and aerosol. For this, the backscatter at 532 nm, the backscatter ratio between the 1064 nm and 532 nm channels, and the midlayer altitude are used. Depending on the classified scene type, further details about the particular class are derived. For *aerosol* classified scenes, a decision tree approach is used for specifying an aerosol type. In

the first step the extinction to backscatter ratio (EBR) is analyzed and compared to EBRs from a database. The database knows six different aerosol classes: desert dust, smoke, clean continental, polluted continental, clean marine, polluted dust, of which each type is linked to a characteristic EBR. In further steps, the depolarization ratio is used to differentiate between particles with similar EBR characteristics. With this method, dust aerosol can be discriminated from hydrated droplets. For *cloud* classified scenes, the depolarization ratio is used directly to determine if the signal was backscattered by liquid cloud droplets or by non-spherical ice crystals (Winker et al., 2009).

For the purpose of this study, we use CALIOP satellite data for investigating cloud and dust vertical structures and type, and as reference for models simulating these. For this application a high reliability of the CALIOP retrievals is crucial. Studies comparing CALIOP aerosol classification to measurements from the AERONET measurement network find a high agreement between both, with best agreement for dust (91% of cases agree in classification) (Mielonen et al., 2009). We hence use CALIOP data as a reliable measure for cloud and aerosol.

We use the Vertical Feature Mask product in the most recent version 4.21, which includes all information from the scene classification, aerosol species derivation and cloud type derivation.

### 3.2.4 Aeronet Measurement Network

We use data from the Aerosol Robotic Network (AERONET) for the validation of model dust data. The AERONET is an international ground-based aerosol monitoring network based on standardized measurements with sun and sky scanning spectral radiometers. Measurements are performed at eight different wavelengths between 340 nm and 1020 nm. Measured radiation is then compared to pre-calculated values for clear-sky conditions in an idealized water vapor free atmosphere. From this, atmospheric optical depth at different wavelengths is calculated (Holben et al., 1998). Optical depth depends on the wavelength to particle size ratio, which can be expressed with the Angström exponent. In the wavelength band of AERONET radiometers, the Angström exponent is large for fine aerosol particles and near zero for coarse particles (Eck et al., 1999). This is used as input for a Spectral De-Convolution Algorithm (SDA), which assumes the aerosol distribution as bimodal and the Angström exponent for large particles as zero. SDA yields separate AOD values for fine (sub-micron) and coarse (super-micron) particles at 500 nm wavelength. The information about AOD for different modes can be used as an estimate for the presence of fine or coarse particles (O’neill et al., 2003). The uncertainty of AOD retrieved via AERONET was evaluated around 0.01 - 0.02 for early versions of the retrieval algorithm (Holben et al., 2001).

For the purpose of this thesis we use level 1.5 SDA data, which is automatically cloud cleared but may not have the final calibration applied. Measurements are only performed under clear-sky conditions, SDA is performed if minimum quality requirements are met. For assessing dust, we use the *Coarse Mode AOD at 500nm*, which captures optical depth from coarse particles at a similar wavelengths as simulated DOD in models.

### 3.3 K-means Clustering

The K-means clustering algorithm is an iterative method which is based on the partition of a set of data into K clusters and the minimization of the sum of squares (Euclidean distances) within each cluster (Hartigan, 1975). The algorithm starts with K pre-selected cluster centers and assigns data points in the neighborhood of the cluster centers to the specific cluster. After assignment of points to clusters, new cluster centers are calculated and points in the neighborhood are again assigned to the closest center. This is repeated until a stopping criteria is reached, typically such that no movement of a point from one cluster to another will reduce the total sum of squares within a cluster, i.e. a local minimum is reached (Hartigan and Wong, 1979). In this study we use the K-means cluster algorithm for clustering events via the 500 hPa geopotential field, see section 6.1.1.

### 3.4 Bootstrapping and Difference of Medians

The bootstrap is a method for estimating the distribution of a test statistic via resampling of the original data sample. It requires no theoretical calculations or knowledge about the real distribution of the test statistic and can be applied no matter how complicated the test statistic is. The bootstrap is based on so-called *bootstrap samples*. Bootstrap samples are created from the original sample by randomly drawing with replacement, so that each bootstrap sample has the same length as the original sample. For each bootstrap sample the test statistic is calculated. Following the central limit theorem, the bootstrap distribution of the test statistic will become normal for a very large number of samples. Selecting quantiles from the bootstrap distribution, confidence intervals for the test statistic can be estimated. For a two-sample problem, the test statistic, i.e. a difference of medians between two groups, is evaluated for each bootstrap replication. For the example of medians, this results in a bootstrap distribution which is close to zero if medians are the same, and away from zero if the medians are different. The quantile of the bootstrap distribution which extends over zero can then be used as a confidence measure for the difference in medians (Efron and Tibshirani, 1994).

### 3.5 Brightness Temperature from Model Variables

The ICON model does not provide an output variable for BT. For comparison of ICON model data to satellite data, we hence calculate a simulated BT from ICON data. For this we modify an algorithm from *wrf-python* package, which contains a collection of diagnostic and interpolation routines initially developed for the use with the Weather Research and Forecasting (WRF-ARW) Model (Ladwig, 2018). The algorithm takes into account air temperature, pressure, water vapor mixing ratio, cloud water mixing ratio, ice mixing ratio and yields simulated cloud optical depth from the cloud top downwards. The algorithm then derives the height at which a threshold of cloud optical depth is exceeded. This height is then defined as the cloud top height. The temperature at the respective cloud top height gives the cloud top temperature. We use the default optical depth threshold of 1.0 for the calculation of cloud top height. For clear-sky cells we take surface temperature as the radiative temperature, and combine it with the calculated cloud top temperature to a simulated BT.



## 4 Event Selection and Data Verification

For the purpose of this thesis, we perform a case study for improving our understanding of model errors during dust events. We examine several recent dust events as possible candidates. For a general statistical investigation, we construct an event catalog of dust outbreaks. This chapter outlines the underlying selection criteria for both the case study and the event catalog. In a subsequent step we verify dust model data against measurement data for the event catalog.

### 4.1 Events in Spring 2021 and Selection for Case Study

During the early months of 2021, several events occurred during which large amounts of Saharan dust were transported towards Central Europe (Hoshyaripour 2021, Magnusson et al. 2021):

- During 05–07 February under mostly cloudy conditions, with highest DOD and extend of the dust plume being reached over France, Switzerland and southern Germany late on 06 February
- During 21–26 February under increasingly cloud free conditions, with highest DOD initially being reached on 22 February over France, Switzerland and the Benelux countries, and with dust concentrations remaining clearly above average over large parts of central and eastern Europe until 26 February
- During 01–03 March under conditions with cloudy as well as cloud-free areas, with the highest DOD and extend of the dust plume being reached over France, Switzerland, the Benelux countries and southern Germany on 03 March
- During 29 March – 01 April under mostly cloudy conditions, with highest DOD being reached on 30 March over the Iberian peninsula

During all events, model quick look data of simulated brightness temperature suggested an underestimation of cloudiness, most notably during the events in March 2021. Early studies conclude that it is not yet clear if the observed cloud errors are related to model errors in dynamics or moisture, or whether missing aerosol interactions in the model play a role (Magnusson et al., 2021). For evaluating the question whether dust is the cause for these model errors, i.e. via missing implementations of aerosol interactions, we select an event with varying cloudiness throughout the dust plume. This provides us with multiple options for analysis, and the examination of model errors during the presence or absence of dust. Likewise we aim to maintain a connection to observed errors in the

photovoltaic forecast over Germany. The event in the beginning of March fulfills these criteria best. We hence select this event for an in-depth case study within this thesis. In the following the event is referred to as *03 March event*, due to strongest pronounced model errors on 03 March.

## 4.2 Event Catalog and Selection Criteria

For a general assessment of the effect of Saharan dust on weather forecast over Europe, representative data for these weather situations is required. Especially for a quantitative analysis, numerically consistent data is essential. For the validation of data from operational models against satellite data, changing model versions, changing satellite instruments or retrieval algorithms can limit data consistency. Due to the limited availability of consistent satellite data, we restrict our analysis to the period from 2018 to mid 2021.

We select dust events over Europe by exceedance of a background DOD threshold at a number of model cells. For this we use dust data from the CAMS near-real-time forecast at initialization time (see section 4.3 for a validation of this data). We use a threshold value of 0.1, which is consistent with thresholds used for differentiating from background aerosol (Holben et al., 1998). Additionally we only select events where a large number of model cells shows increased DOD, for which we compare the median DOD throughout a selected area to a manually tuned threshold. In addition we limit the relevant area to Germany and selected countries in Central Europe (Austria, Belgium, France, Luxembourg, Netherlands, Switzerland, see figure 4.1), to ensure similar synoptic conditions over the analysis area and to provide analysis which can be connected to PV forecast. With this we also limit analysis to land areas and avoid possible satellite biases between land/sea surfaces.

This leads to the following event selection criteria:

- Number of cells with  $\text{DOD} > 0.1$  is greater than 25% of total cells in selected area
- Median DOD of all cells in selected area is greater than 0.075

We apply the criteria to the area of Germany for the period from 2018 until mid 2021 for each day at 00 and 12 UTC. This yields the selection of 11 individual days. We also apply the criteria to the restricted area in Central Europe as defined above, which yields the selection of 33 days. For obtaining the final event catalog we merge the selected days for both areas, resulting in a total number of 38 days. The so selected dates show clusters of several consecutive days, which in the following are called *events*. The 38 selected days form 21 events. For quantitative data analysis we use data from all 38 days, for synoptic analysis we only use the first day of each event. Finally we manually analyze all selected days for other prominent aerosol species over the selected area in Central Europe, to ensure mineral dust being the dominant aerosol. The selected days are summarized in table 4.1.

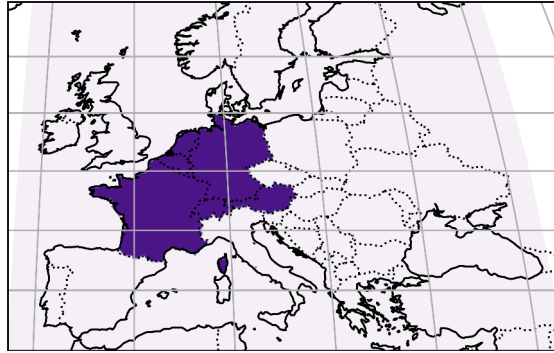


Figure 4.1: Limited area for event selection and analysis.

Selected Events Germany	Selected Events Europe
2018-04-09	2018-04-07
2018-04-13	2018-04-08
2019-06-11	2018-04-09
2019-06-12	2018-04-23
2019-06-15	2018-05-26
2020-02-29	2018-05-27
2021-02-22	2018-05-28
2021-02-23	2018-06-11
2021-03-03	2018-08-07
2021-03-04	2019-04-22
2021-06-20	2019-04-23
	2019-06-14
	2019-06-15
	2019-06-25
	2019-06-26
	2019-06-27
	2019-07-24
	2019-07-25
	2019-10-23
	2019-12-17
	2020-01-23
	2020-05-10
	2020-05-13
	2020-11-07
	2021-02-06
	2021-02-22
	2021-02-23
	2021-03-02
	2021-03-03
	2021-04-01
	2021-06-17
	2021-06-19
	2021-06-20

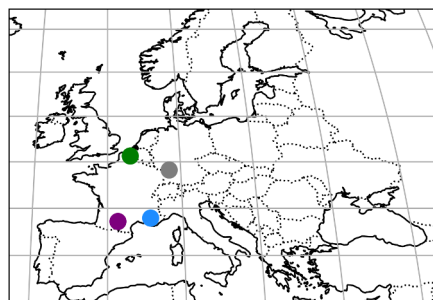
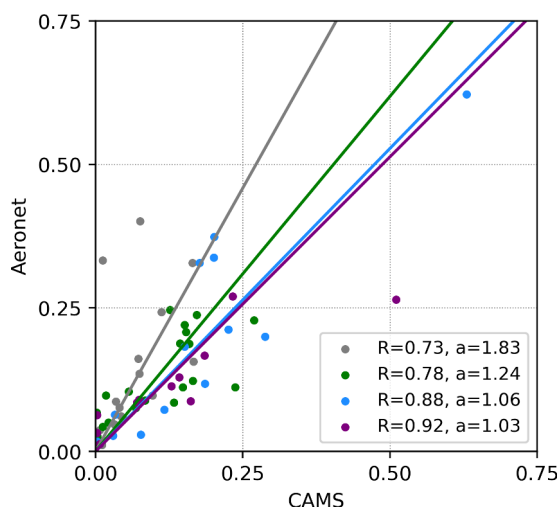
Table 4.1: Selected days for the event catalog from application of the selection criteria to the area of Germany and the restricted area in Central Europe. The event catalog combines both lists.

### 4.3 Validation of CAMS Dust Data

Recent studies have shown that the CAMS dust analysis captures AOD well over Europe, with a mean bias error of -0.02 relative to Aeronet measurements (Gueymard and Yang, 2020). For obtaining a measure for the representativeness of CAMS dust simulations over the selected area, we compare DOD from the CAMS model to AOD measurements from the Aeronet measurement network. We select the stations Karlsruhe, Lille, Toulouse and Haute-Provence, which are distributed across the restricted analysis area (figure 4.2b), and take the DOD value from the CAMS near-real-time analysis at the model cell closest to the Aeronet station for each day in the event catalog. For the same stations we take Aeronet measurements of 500 nm coarse mode AOD, which serves as a measure for DOD. As the Aeronet measurements are performed with a stationary photometer, the source of the measured value is highly local. In contrast, model data only provides one value for the whole model grid-cell every 3 h. To compensate for this, we calculate a 3-hourly averages from the Aeronet data, which is consistent with the approach used by Gueymard and Yang (2020). We then compare the 3 h mean value from Aeronet to the CAMS value. We perform all comparisons at 12 UTC. As Aeronet only retrieves data during clear-sky conditions, we get fewer days with comparable data than the total number of days in the event catalog. For each station we calculate the Spearman correlation coefficient and the slope of a linear regression through the origin, as a measure for the deviation from ideal agreement between model and measurement data (in an ideal case, the slope would be 1).

The scatter plot in figure 4.2a shows a generally good agreement between model DOD and Aeronet measurements. Most daily values are located around an ideal diagonal with the slope 1. The model on average shows slightly lower values than the measurements, with all regression slopes being greater than 1. This can be a systematic error as CAMS values represent a large area (which tends to smooth extreme values) compared to the narrow slice from 3 h averaged Aeronet data. In addition, Aeronet measurements of 500 nm coarse mode AOD include other aerosol species besides dust, which can lead to higher values than the dust-only AOD (DOD) from the model. For few individual days the model shows far lower values compared to Aeronet for Karlsruhe, as well as higher values for Toulouse. Manual investigation of the dust forecast for these particular days and comparison to Aeronet data suggests the model simulating slightly different dust transport patterns and subsequently concentrations, compared to the measurements.

In summary, the comparison of CAMS DOD model data to Aeronet measurement data suggests generally good agreement between model and measurement data for the selected stations, with only few disagreements for individual events or at individual stations. Assuming the Aeronet measurements to be the closest representation of the actual real world conditions, we conclude the CAMS DOD data to be a representative measure for dust concentrations over the restricted analysis area and the dates in the event catalog. Due to this good representation, we further conclude the solely use of model DOD for the selection of dust events over Central Europe to be justified.



(a) Coarse mode DOD at 500 nm from Aeronet versus DOD from CAMS, Spearman correlation coefficient and slope of regression line for the specific station

(b) Locations of selected Aeronet stations

Figure 4.2: Verification of CAMS DOD versus coarse mode DOD at 500 nm from Aeronet for selected stations in the restricted analysis area and all events from the event catalog. Stations include Karlsruhe (grey), Lille (green), Toulouse (purple), Haute-Provence / OHP (blue).



## **5 Case Study: Dust Outbreak on 03 March 2021**

During February and March 2021 several events occurred during which high loads of Saharan dust were transported towards Western and Central Europe (Hoshyaripour 2021, Magnusson et al. 2021). The event in the beginning of March was strongest pronounced over Central Europe on 03 March, and stands out due to large and spatially consistent model errors in cloudiness.

This chapter provides an in-depth analysis of the 03 March dust event and forms a basis for the systematic analysis of dust events. Firstly, we give an overview about the synoptic conditions leading to the 03 March event. Secondly, we analyze dust transport to Central Europe during this event and discuss characteristic patterns. Thirdly, we compare model temperature and moisture profiles to radiosonde data for assessing possible errors in moisture representation in the model. We also compare model data of cloudiness and surface radiation to satellite retrievals and discuss matching patterns with the dust plume. Finally, we compare station data of surface radiation data to satellite retrievals, and to model data from runs with different complexities of aerosol implementations, in order to assess shortcomings within satellite retrievals and model forecast improvements and with inclusion of direct aerosol effects.

For the case study, we use a variety of data sources from measurement platforms and models. For a summary of the data products used for this section see table 5.1.

<b>Data source</b>	<b>Variable</b>	<b>Usage</b>
Radiosondes	air temperature dew point temperature	Vertical temperature and moisture profiles
GridSat	brightness temperature	Reference for calculation of model error
Meteosat	cloud mask surface shortwave radiation	Reference for calculation of model error
Calipso	vertical feature mask	Vertical cloud and aerosol profile
ECMWF IFS (operational)	geopotential sea level pressure brightness temperature surface shortwave radiation	Synoptic overview, analysis of model error
CAMS (near-real-time)	geopotential integrated dust optical depth	Analysis of dust transport
ICON (operational)	surface shortwave radiation air pressure moisture (qv, qcld, qice) air temperature	Analysis of model error
ICON-ART (pre-operational)	surface shortwave radiation air pressure moisture (qv, qcld, qice) air temperature extinction from dust	Analysis of dust transport, vertical profiles, model error

Table 5.1: Summary of data products and variables used for the the case study.

## 5.1 Synoptic Overview

At the beginning of March (figure 5.1a), large parts of Europe are located under the influence of a pronounced high pressure system with its center over Germany. This forms an omega-like situation over Central Europe and causes large scale subsidence with stable clear-sky conditions during day. West from the high pressure system, a trough is spanning from a low pressure region over the Biscay sea via the western Iberian peninsula towards northwestern Africa. This results in enhanced pressure gradients and surface wind speeds over the Atlas mountains and central Algeria around 28 February and 01 March. On 01 March, stations record gusts in Er-Rachidia, Morocco of up to 59 km/h and gusts in Tozeuz/Nefta, Algeria of up to 65 km/h, a favorable condition for the emission of Saharan dust from those regions. With the southwesterly flow over the western Mediterranean, subtropical air masses and Saharan dust are transported northwards.

On 02 March (figure 5.1c), the high pressure systems starts to weaken at its northern edge, and changes to a ridge with its axis is slowly shifting eastwards. The upper low pressure zone over the Biscay sea increasingly decouples from the general flow and forms an upper cut-off low. Central Europe is still largely affected by subsidence, maintaining clear-sky conditions during day. In the southerly flow over the western Mediterranean, which carries Sahara dust and moisture, a high cloud shield forms (figure 5.1d), which reaches the eastern Iberian peninsula and southern France during the course of the day.

From 02 to 03 March (not shown), the high pressure system over Central Europe strongly weakens and the upper low pressure region shifts from the Biscay sea northeastwards, leading to the formation of a short wave trough over the British isles. This changes the winds in the high troposphere to south-westerly / westerly directions. At the same time first patterns of a trough over Scandinavia develop. On 03 March (figure 5.1e), the southern parts of Central Europe are still under the influence of the weakening ridge, while northern parts are under increasing cyclonic influence. The Satellite pictures show the high cirrus cloud shifting further northeast, finally extending from the Iberian peninsula over central France and the Alps to Germany and the western Czech Republic (figure 5.1f). The development of this largely extended cirrus is remarkable, as the general situation indicates weak synoptic forcing, and the short wave trough (axis) over the British isles does not extend far into the region where the cirrus forms. The shortwave trough however leads to enhanced wind speeds and south-westerly / westerly wind directions in the mid and high troposphere, favoring the advection of additional dust in these layers. This is discussed in more detail in section 5.2.

Towards 04 March (figure 5.1g), the high pressure dominance over Central Europe rapidly declines. The trough over Scandinavia strongly deepens, leading to a northerly flow over the northern parts of Central Europe and a westerly flow over the southern and eastern parts. The westerly flow spreads the aged subtropical air, which still carries Saharan dust, over Eastern Europe and the Balkans. With the increasingly northerly flow, polar air is advected southwards and forms precipitating cold fronts which cross Germany during 04 March. This leads to washout of the remaining Saharan dust, ending the dust event in Central Europe.

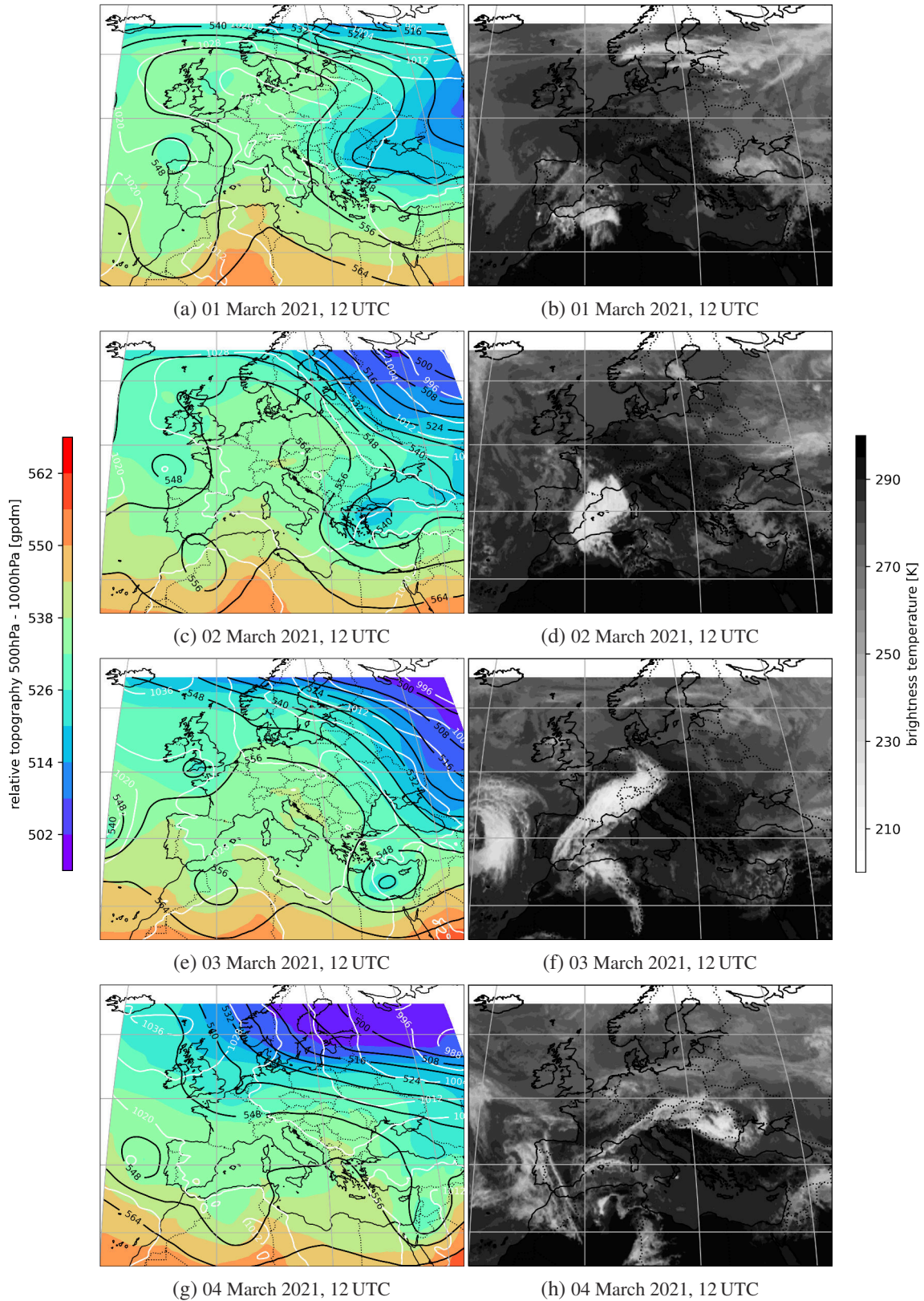


Figure 5.1: Synoptic overview in the beginning of March 2021. Geopotential and pressure (left) from ECMWF analysis: Mean sea level pressure (white, in hPa), 500 hPa geopotential (black, in gpdm), relative topography between 500 hPa and 1000 hPa (filled contours, in gpdm). Brightness temperature (right) from GridSat satellite products: Low temperatures indicate emitting objects in high altitudes, typically clouds.

## 5.2 Dust Transport towards Central Europe

Dust properties are connected to the chemical composition of dust, which can change due to chemical reactions within the atmosphere. Processes such as aging alter the efficiency of dust for acting as CCN or INP (see section 2.1). The residence time and transport path in the atmosphere can hence affect effects of dust via chemical reactions during transit. In this chapter we study the transport patterns which advect mineral dust to central Europe during the 03 March event. We analyze forecast data from CAMS and ICON-ART models, with 12-hourly (CAMS) respectively daily (ICON-ART) reinitialization, leading to maximum leadtimes of less than 24 hours. For validation, we compare this data to measurements from CALIOP of the CALIPSO satellite, from the overpass on 03 March between 13:04 UTC – 13:13 UTC (30–60°N).

### General Transport Patterns and Validation versus CALIPSO

For a first assessment of dust transport we analyze the total DOD from model forecasts. Figure 5.2 shows DOD from 01 March to 04 March in the CAMS model. It shows transport of dust via Spain and the western Mediterranean (01 March), via France (02 March) towards Germany and large parts of Central Europe (03 March). On 04 March DOD is highly reduced, which fits with the change in weather situation which spread dust towards Eastern Europe and the Balkans. Starting from 04 March 00 UTC, remaining dust is washed out via precipitation over large parts of Central Europe. Figure 5.3 shows DOD from 02 to 03 March in the ICON-ART model. Compared to CAMS, ICON-ART shows a slightly higher background DOD and broader extent of the dust plume. However the main features in spatial coverage as well as temporal evolution of the dust plume are consistent between the models.

For validation of the dust patterns as simulated in the models, we use data from the CALIPSO overpass on 03 March early afternoon, which is shown in figure 5.4. The vertical feature mask shows a high cirrus cloud band between 42°N and 48°N, with a cloud top of 11 to 12 km and a layer of dust aerosol between 48°N and 53°N, reaching into altitude of about 5 km. South from the Alps (south from 42°N), a low aerosol layer is recorded, reaching altitudes of about 2 km and only consisting of dust at its northern edge. Around 54°N, isolated pixels of dust aerosol are recorded in about 9 km altitude. Below the cirrus cloud layer, the lidar signal is totally attenuated and no aerosol information was derived.

Comparing model DOD from figures 5.2 and 5.3 with CALIPSO data, suggests a good agreement for the zonal extend of the dust plume between model simulations and the CALIPSO retrieval. The cold cirrus cloud which is recorded in GridSat BT (see figure 5.1f) is consistent with the CALIPSO profile, but prevents from the retrieval of aerosol information below the cloud layer. Individual dust aerosol pixels north from the cirrus cloud suggest the presence of dust in higher altitudes up to 9 km, which would mean a vertical overlap of dust with the cirrus cloud layer. The robustness of individual pixels however can be called in question, hence further analysis will examine the vertical structure of the dust cloud in more detail.

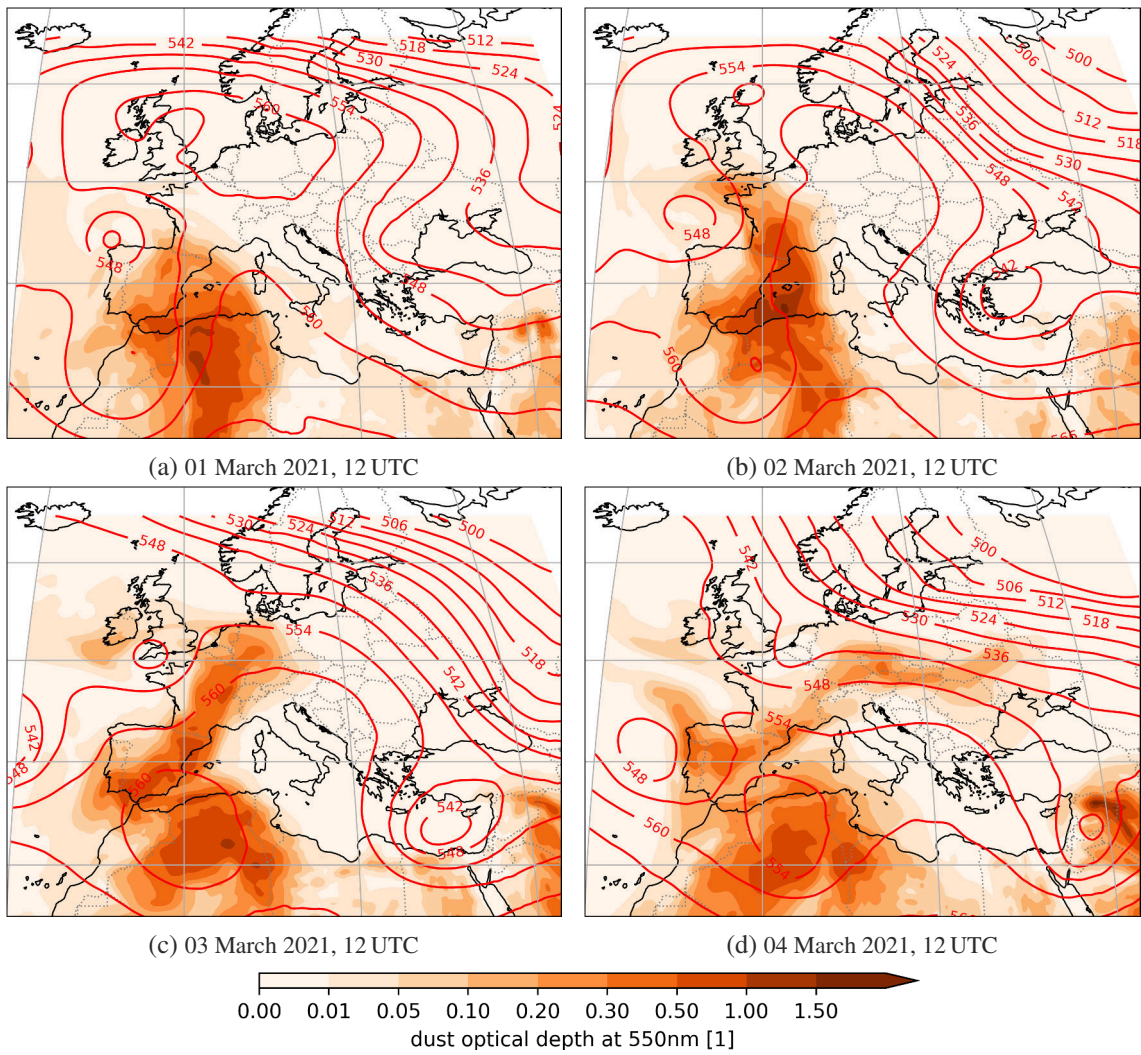


Figure 5.2: Dust optical depth (filled contours) and 500 hPa geopotential (red, gpm) over Europe from 01 to 04 March 2021 from CAMS near-real-time forecast.

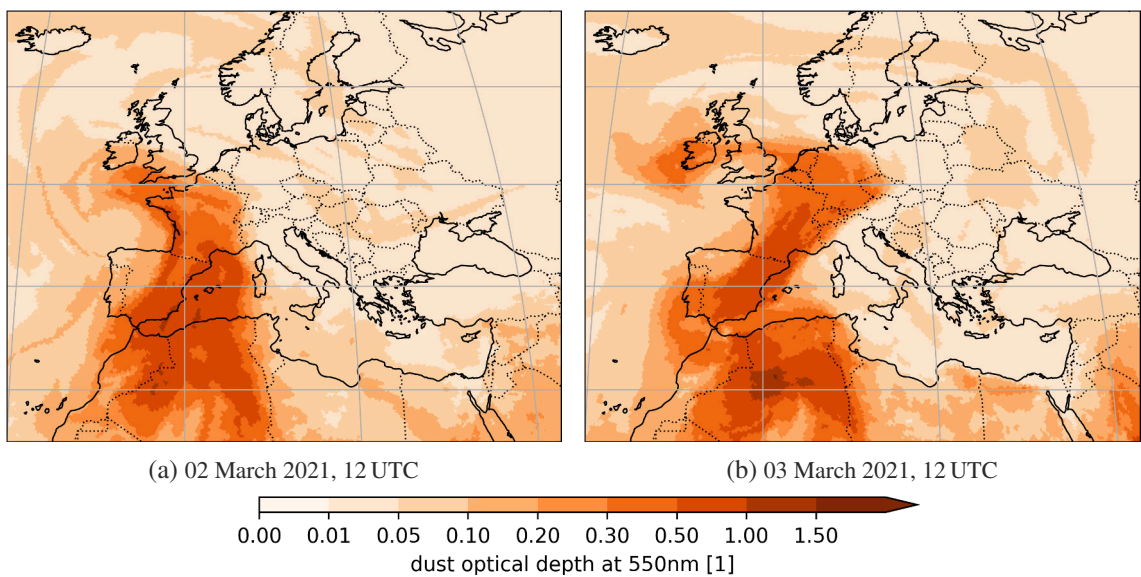


Figure 5.3: Dust optical depth (filled contours) over Europe from 02 to 03 March 2021 from ICON-ART quasi-operational forecast.

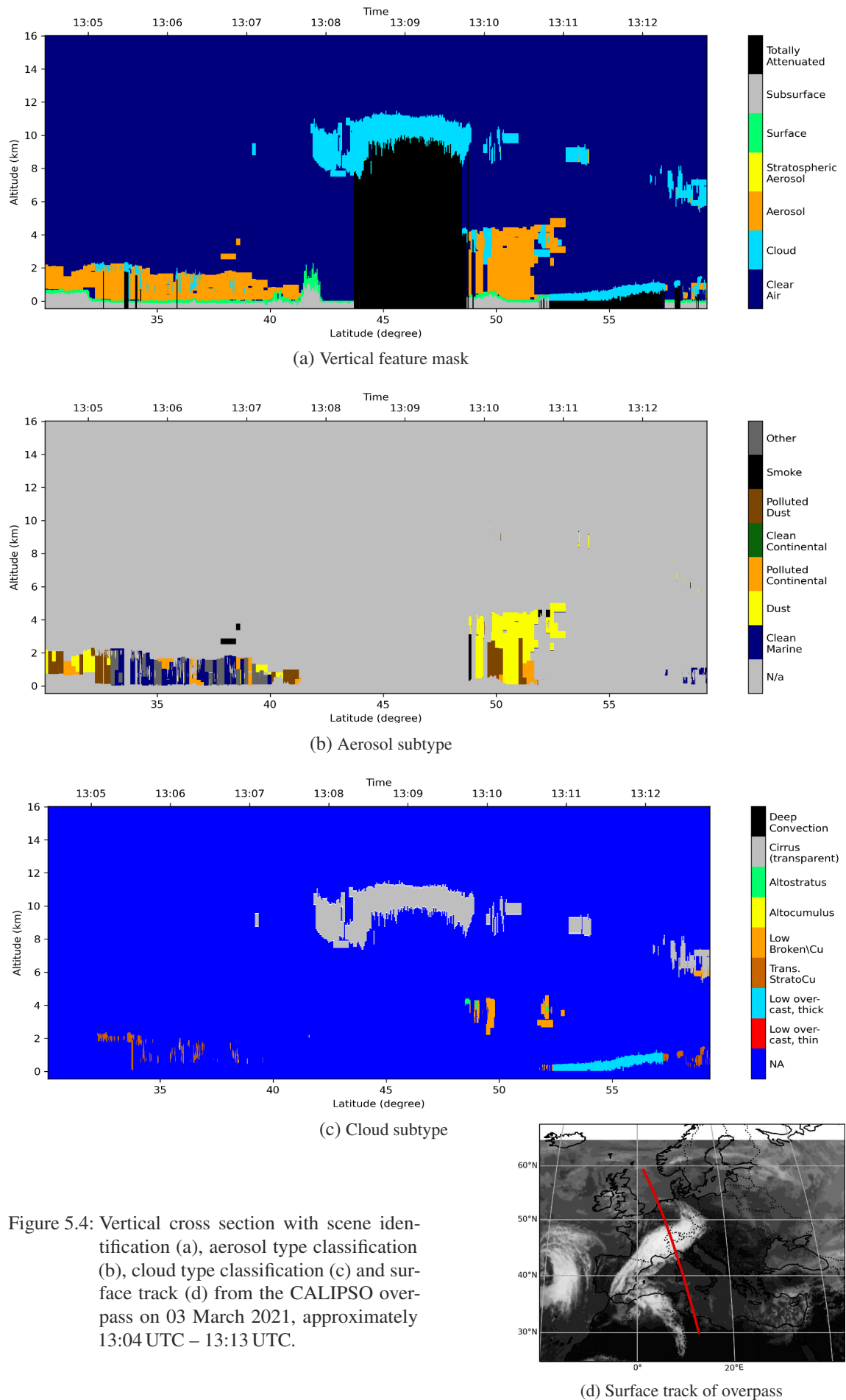


Figure 5.4: Vertical cross section with scene identification (a), aerosol type classification (b), cloud type classification (c) and surface track (d) from the CALIPSO overpass on 03 March 2021, approximately 13:04 UTC – 13:13 UTC.

## Vertical Structure of the Dust Plume and Clouds

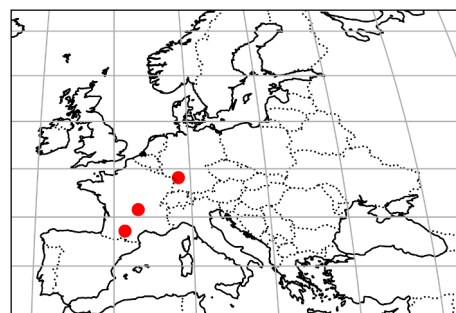
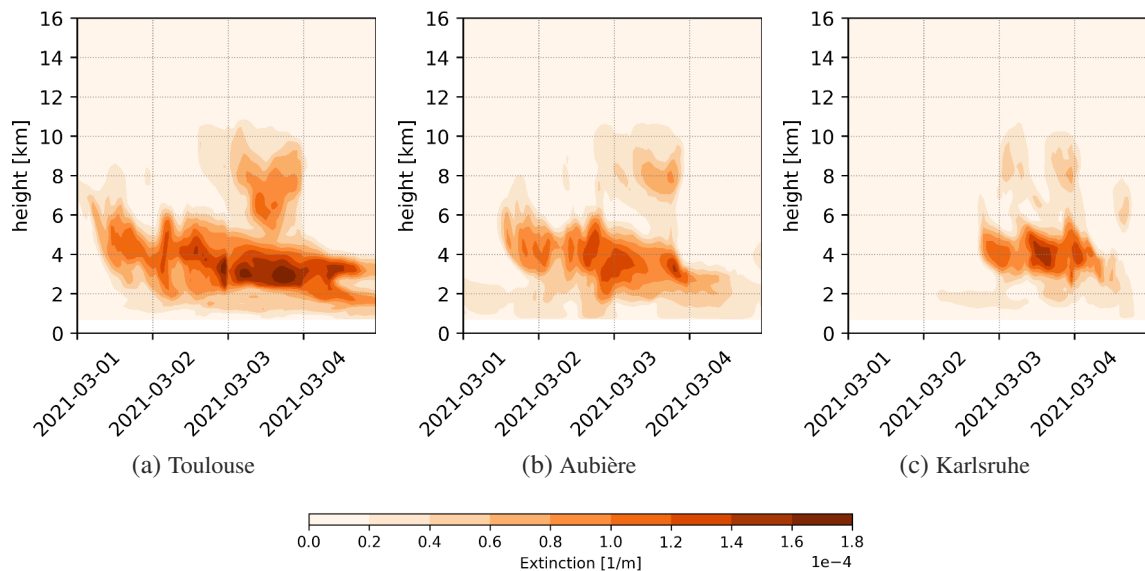
For assessing a potential overlap of dust and cirrus clouds, an indication for interactions between dust and cloud properties, we examine the vertical structure of the dust plume. The CALIPSO profile in figure 5.4 shows individual pixels of dust, which suggests the presence of dust in layers up to 9 km but does not provide sufficient robustness for this. As model data has shown good agreement in horizontal extend of the dust plume compared to CALIPSO measurement data, we use ICON-ART for accessing the vertical structure of the dust plume. ICON-ART provides dust aerosol extinction per model layer, which we normalize with layer thickness for obtaining an intercomparable measure correlated with aerosol concentration.

Examining the formation of the dust plume, we study its evolution over time at selected stations. As shown in figures 5.2, 5.3, dust was advected via Spain and the western Mediterranean via France towards Germany. We hence choose the stations Toulouse, Aubière and Karlsruhe along the dust transport route. Figure 5.6 shows a temporally consistent dust layer below 6 km, first arriving in Toulouse early on 01 March, in Aubière around 01 March midday and reaching Karlsruhe late 02 March. At both Toulouse and Aubière, the plume is temporally consistent, showing only moderate variations in extinction and vertical extend but a temporally continuous dust band between about 2 and 6 km of altitude. This suggests the advection of a large connected dust plume, with little convection occurring within the plume. On 02 March, the model shows dust in Toulouse and Aubière also in altitudes up to about 10 km. For Karlsruhe it also shows dust in this altitude early on 03 March. The temporal evolution of the dust layer vertical thickness does not show a vertical expansion of the low dust layer, but a tendency for decreasing plume top height over time for the low dust layer. Dust in high altitudes above 6 km shows a rapid increase over time without clear spatial connection to the low dust layer (below 5 km on 03 March) and suggests the transport of high dust via advective rather than convective processes.

For further examination of dust transport in different altitudes, we divide DOD into DOD from 5000 m and below and DOD above 5000 m. This altitude threshold is consistent with the layers in dust forecast for selected stations during 03 March (figure 5.6). The temporal evolution of low (5000 m and below) and high (above 5000 m) layer DOD is shown in figure 5.7. From figures 5.7a–c it can be seen that a low dust layer extending from the British isles over France, Spain and the western Mediterranean is already present on 02 March 12 UTC (figure 5.7a), reaching Germany by 02 March 18 UTC (not shown). Advection towards Germany happens mainly via France and the Benelux countries (figures 5.7b–c). From figures 5.7d–f the transport of dust in high altitudes can be seen, which shows a different and more direct advection route compared to the low dust layer. On 02 March 12 UTC (figure 5.7d) most high dust is still located over the western Mediterranean, being advected over southern France by 02 March 18 UTC (not shown). Transport towards Germany occurs mainly over the Alps (figures 5.7e–f), on a more direct transport route than the low dust layer of which most dust is advected around the Alps. This fits to the synoptic situation observed during 02–03 March (see section 5.1, figure 5.1c,e), with increased wind speed and westerly / southwesterly wind directions in the mid and high troposphere due to the upper level low pressure region over the Biscay sea, and the connected short wave trough developing over the British isles. We conclude that the ICON-ART model shows two layers of dust for the 03

March event, with advection of the low altitude dust via a transport route around the Alps and a comparably faster advection of high altitude dust on a more direct transport route over the Alps towards Germany.

For assessing consistency of a high dust layer with CALIPSO profiles, we simulate vertical profiles from ICON-ART data along the CALIPSO overpass from 03 March. For this we include extinction from dust, total cloud moisture content (water + ice), saturation over water and calculated cloud top height (see section 3.5), which is shown in figure 5.8. On 02 March 12 UTC (figure 5.8a), only a low dust layer can be seen, reaching altitudes of about 5 km and only exceeding this over the Alps. On 02 March 18 UTC (figure 5.8b) a region of high extinction from dust "pops up" around 27°N and 8 km altitude, without showing a connection to the low dust layer hence suggesting advection rather than convection the underlying process of transport. This fits with the identification of dust layers as shown in figure 5.7. Dust in altitudes up to 11 km increases until 03 March 12 UTC (figure 5.8e).



(d) Locations of the stations, from West to East: Toulouse, Aubière, Karlsruhe.

Figure 5.6: Extinction from dust for selected stations in Europe from 01 to 04 March 2021 from ICON-ART quasi-operational forecast.

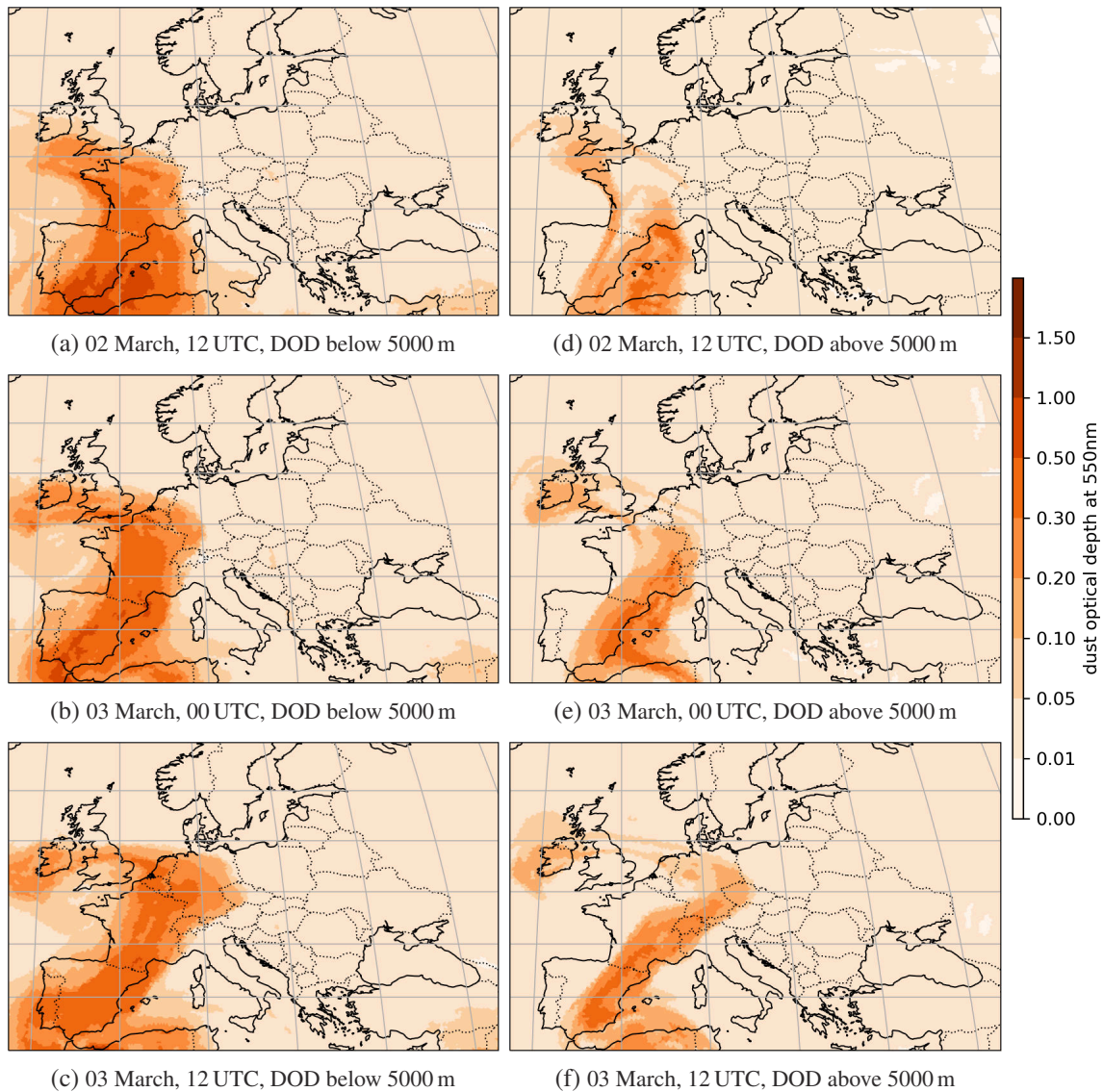


Figure 5.7: DOD over Europe from 02 to 03 March 2021 in different altitudes; 5000 m and below (a–c) and above 5000 m (d–f). Data from ICON-ART quasi-operational forecast.

Comparison of the simulated cross section on 03 March 12 UTC (figure 5.8e) with the CALIPSO overpass from around 13 UTC (figure 5.4) shows a very good alignment of recognizable features. The model reproduces the low dust layer with embedded broken cumulus clouds as seen in CALIPSO data in altitudes up to 5 km between  $48^{\circ}\text{N}$  and  $53^{\circ}\text{N}$ , however with the clouds missing but high humidity within the dust layer. Both satellite retrieval and model data show the cirrus cloud in up to 10 km around the same latitudes and cirrus clouds in up to 8 km at  $60^{\circ}\text{N}$ , the dense low overcast north from  $52^{\circ}\text{N}$  as well as the mixed aerosol layer with isolated clouds in up to 2 km south from  $41^{\circ}\text{N}$ . Even the isolated dusty pixels in the CALIPSO retrieval in 9 km around  $54^{\circ}\text{N}$  align with dust patterns as calculated by the model. In contrast, the prominent cirrus layer in CALIPSO data in up to 11 km between  $42^{\circ}\text{N}$  and  $48^{\circ}\text{N}$  is missing almost completely in the model. Instead the model shows high extinction from mineral dust. The same applies for the cirrus clouds in up to 9 km around  $54^{\circ}\text{N}$ , where the model shows high extinction from mineral dust and CALIPSO shows isolated dusty pixels.

Due to the very good agreement of various features in the CALIPSO retrieval and ICON-ART data, we conclude that the model is generally capable of reproducing the weather situation and many vertical structures during 03 March. The very good agreement of model dust data with the CALIPSO profile suggests that the model is also capable of reproducing dust transport and resulting vertical structures. From this we conclude that the dust plume between  $42^{\circ}\text{N}$  and  $48^{\circ}\text{N}$  in altitudes of up to 11 km is a realistic feature, and likely is simply hidden in the CALIPSO retrieval by the attenuation from the high cirrus cloud layer. The disagreements in cloudiness between model and satellite all align with regions with high DOD, and are especially prominent for cirrus clouds and the high dust layer above 5000 m. We conclude that the mineral dust in high altitudes is most likely a major cause of these model errors in cloudiness.

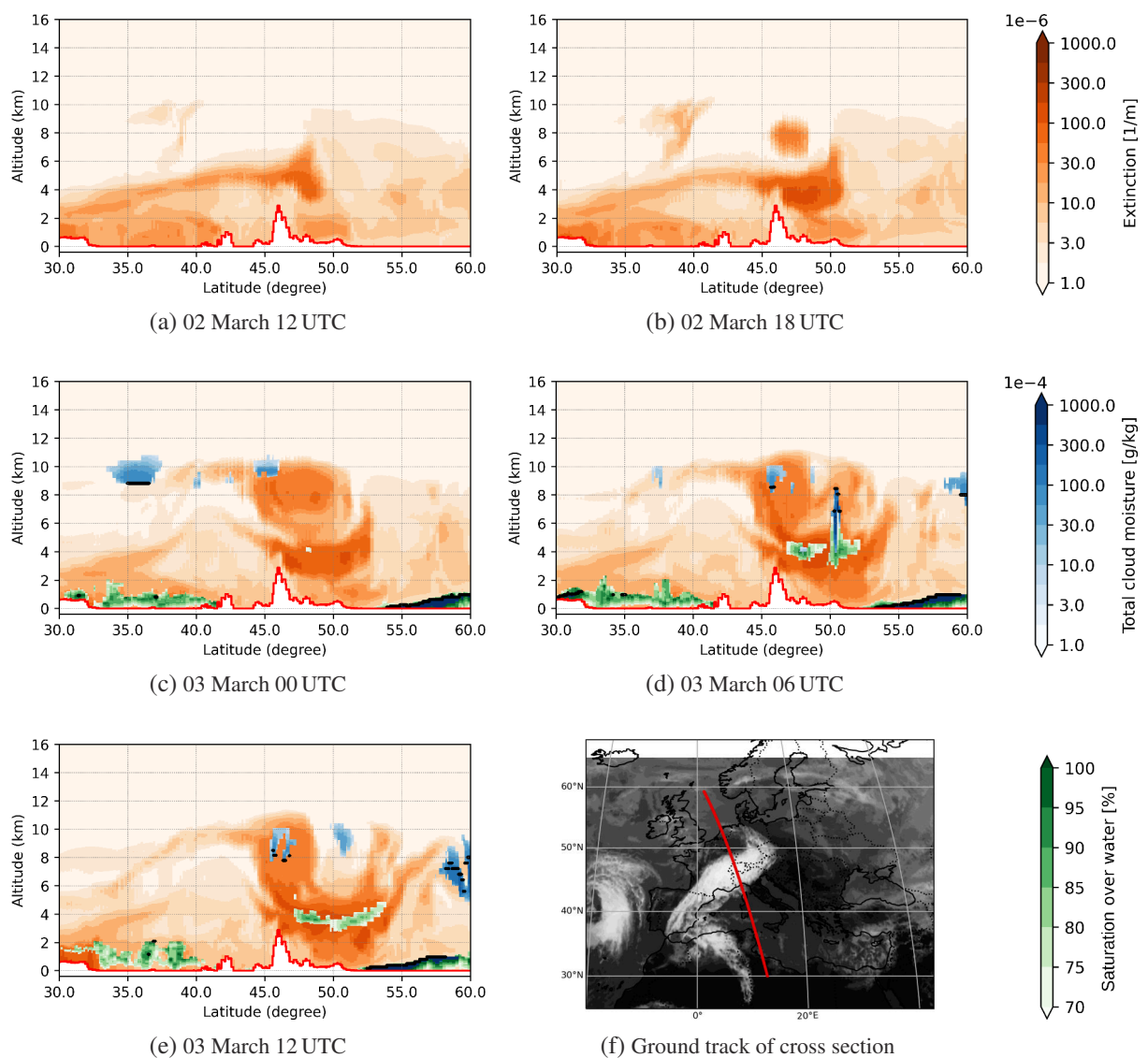


Figure 5.8: Vertical cross sections on 02 and 03 March along CALIPSO track from ICON-ART quasi-operational forecast. Extinction from dust aerosol in orange, total cloud moisture (water + ice) in blue, saturation over water in green, calculated cloud top height as black lines and surface as red line. For 02 March, moisture data is not available and not shown.

## 5.3 Comparison to Satellite Data

The previous sections show that the dust plume aligns well with the spatial pattern of cloud errors in the ICON-ART model. Even though ICON-ART provides interactive computation of aerosol and direct aerosol radiative effects (Rieger et al., 2017), the model shows errors in cloudiness. In this section we further analyze model errors during the 03 March dust event, focusing on differences in BT as a measure for errors in cloudiness, and SIS as an indicator for impacts on further meteorological variables. Due to data availability and the deployment in operational weather forecasting, we focus on data from the ECMWF IFS model and perform analysis with ICON-ART only for the time of most pronounced model errors on 03 March 12 UTC.

Figure 5.9 shows an overview about dust transport and cloudiness from 01 to 03 March: Total DOD from the CAMS model (a–c), simulated BT from the ECMWF IFS model (d–f), BT from GridSat satellite products (g–i), and differences between model and satellite (j–l). Comparing cloud patterns over Scandinavia, the Iberian peninsula, the Bay of Biscay or the eastern Mediterranean, there is a good agreement in cloud structures between model and satellite throughout the period from 01 to 03 March. This indicates that the model is generally capable of reproducing the synoptic situation as well as many cloud structures. Focusing on the regions with high DOD, model and satellite differ increasingly from 01 to 03 March. The high cirrus cloud which can be seen from satellite pictures is largely underestimated in the model. On 02 March the cirrus cloud layer is located over the western Mediterranean and is only weakly pronounced in the model. On 03 March the cirrus cloud layer extends from the Iberian peninsula until Germany and is almost invisible in the model. The discrepancies between model and satellite are pronounced in the area of high DOD and reach values up to 75 K. This suggests the high cirrus cloud layer to be highly underestimated or mostly missing in the model. This also matches with the results from vertical analysis and comparison to the CALIPSO overpass as examined in section 5.2, which found agreement between dust in the high troposphere and missing cirrus clouds in the model.

The ICON-ART model, which in contrast to the ECMWF IFS model includes prognostic calculation of aerosol properties as well as the direct aerosol effect, equally underestimates the cirrus cloud in the region of high DOD on 03 March, as shown in figure 5.10. ICON-ART shows high clouds in a fraction of the dust plume, but largely underestimates the horizontal extend of the cirrus cloud compared to the satellite. For both ECMWF IFS and ICON-ART models, the errors occur in model forecast (12 UTC, figures 5.9, 5.10) as well as in model analysis respectively at the time of model initialization (daily at 00 UTC, not shown).

Cloud cover and cloud properties play an important role for the radiative budget in the atmosphere (Boucher et al., 2013). Consequentially, model errors in cloudiness can lead to errors in radiative quantities. For assessing this, we investigate errors in SIS. We also use SIS as a measure for error propagation into further meteorological quantities such as air temperature. Radiation data from ECMWF IFS model is given as accumulated values, which we restructure for gaining 3 h mean values. SIS satellite data from SEVIRI on MSG is provided as instantaneous data every 30 min, which we average over 3 h periods for gaining a measure comparable to the model values. For both model and satellite, we assign the 12 UTC time to the period 12 to 15 UTC.

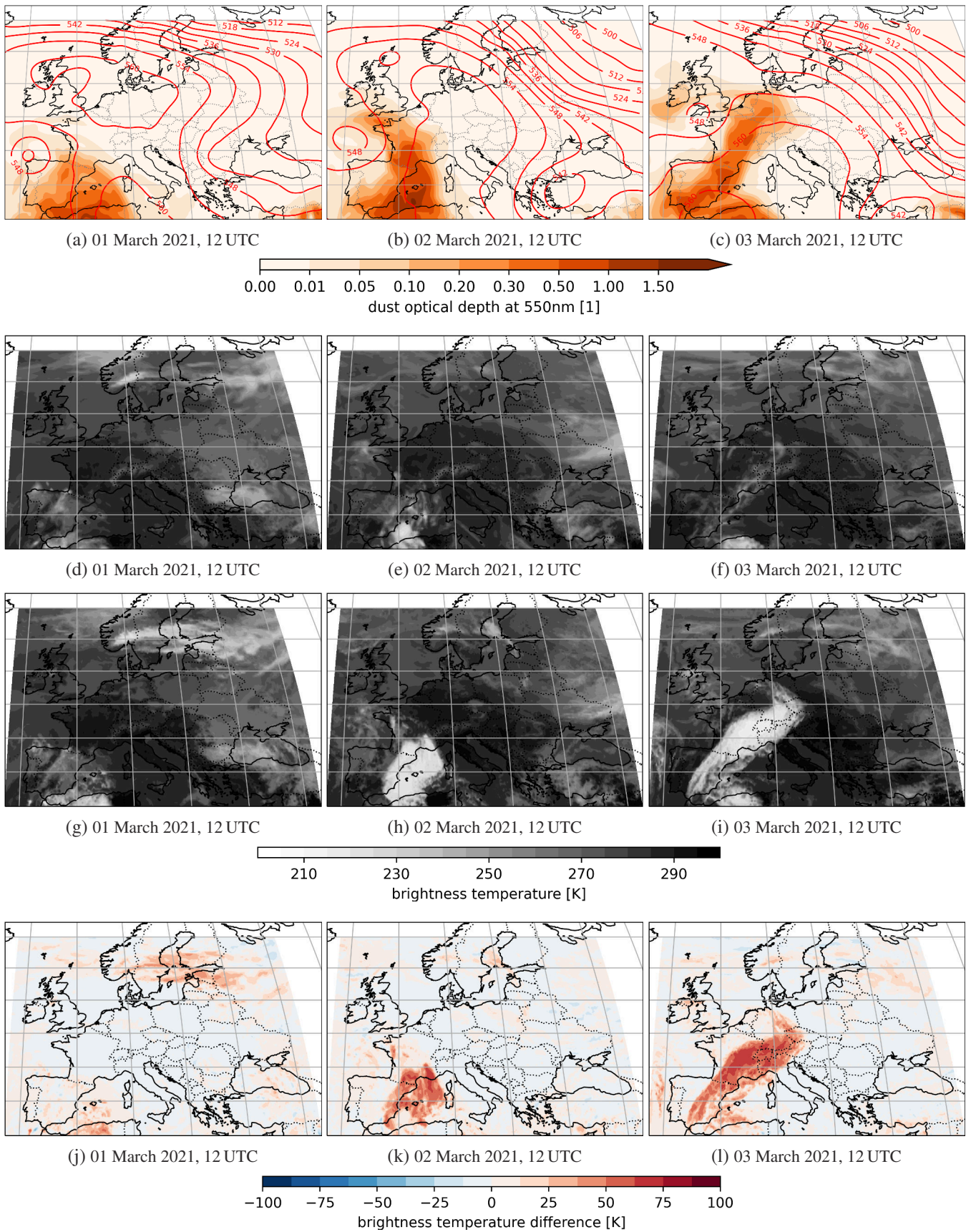


Figure 5.9: Overview about dust transport and cloud properties from 01 to 03 March 2021. DOD and 500 hPa geopotential in CAMS model (a–c), simulated BT from ECMWF IFS model (d–f), BT from GridSat satellite product (g–i) and brightness temperature difference between model and satellite values (j–l).

Figure 5.11 shows SIS from 01 to 03 March as simulated by ECMWF IFS model (a–c), SIS derived from SEVIRI on the Meteosat-11 satellite (d–f) and differences between model and satellite (g–i). There is good agreement between model and satellite in clear-sky regions. In areas of low or broken clouds, there are varying patterns of discrepancy between model and satellite, which are mostly related to temporal or spatial shifts of clouds between model and satellite. These errors increase with increasing forecast leadtimes, resulting in the noisy pattern which is visible in the plots of model to satellite differences. In the area of high DOD and cirrus clouds, namely the western Mediterranean on 02 March, and the area between the Iberian peninsula and Central Europe on 03 March, the model does not show strong reductions in SIS. In contrast, SIS derived from satellite shows largely reduced values in this area. On 03 March, absolute differences between model and satellite reach up to  $300 \text{ W m}^{-2}$  in a spatially consistent area between the Iberian peninsula and Central Europe and exceed  $300 \text{ W m}^{-2}$  at individual locations. This translates into relative model errors in SIS of about 50% in the area of the (missing) cirrus cloud.

SIS and surface temperature are closely linked (Bristow and Campbell, 1984). Consequentially, large model errors in SIS can lead to wrong surface temperature forecasts. Other than for BT and SIS, there are no satellite products available for surface temperature with a high temporal resolution. In this case, station data could be used as reference. For a single event such as this case study, the number of surface observations directly under and besides the cloud is rather limited. In addition, multiple other factors besides SIS can have large impacts on surface temperature, making it difficult to trace back variations in temperature at different stations to the effect of dust. Due to the limited number of station data for this single dust event and due to the large number of other effects on air temperature, we do not perform further error analysis for surface temperature during the 03 March event.

Summarizing spatial analysis of BT and SIS data from model data and satellite products, there is a good agreement between the two data sources, suggesting a reasonable skill of the model to simulate the general synoptic situation of the 03 March event. Large and spatially consistent model errors relative to satellites products occur in regions of high DOD and are most prominent in BT as a proxy for the cirrus cloud layer. Large errors in SIS occur, being spatially consistent with the errors in cirrus cloud cover and providing a link for the propagation of errors into further meteorological quantities such as surface temperature. Comparing to the analysis of the vertical structure of the dust plume in section 5.2, there is a very good spatial agreement between the simulated high dust layer above 5000 m (figure 5.7f) and the region of large model errors.

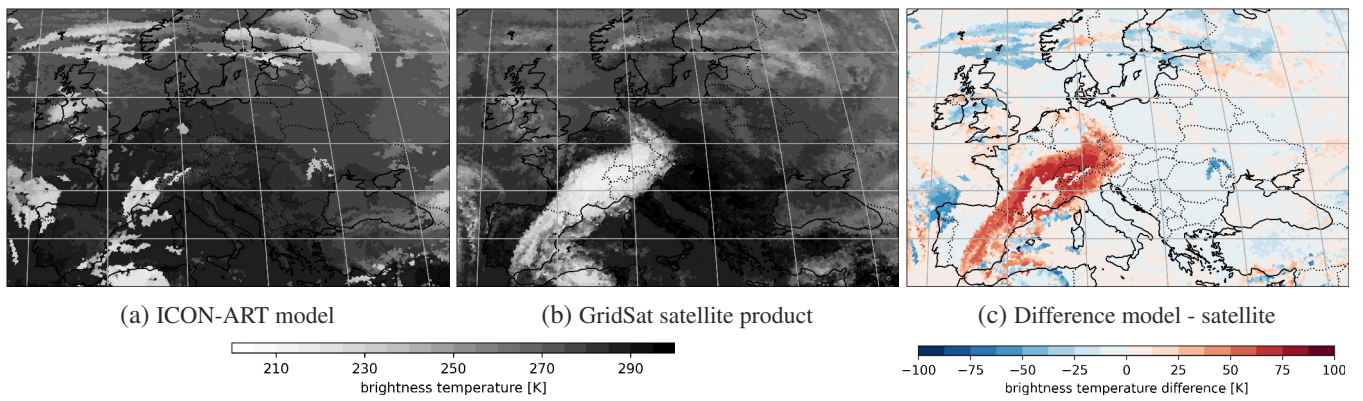


Figure 5.10: Overview about cloud properties on 03 March 2021, 12 UTC in ICON-ART model. Simulated BT from ICON-ART (a), BT from GridSat satellite product remapped to ICON grid (b) and difference between model and satellite values (c).

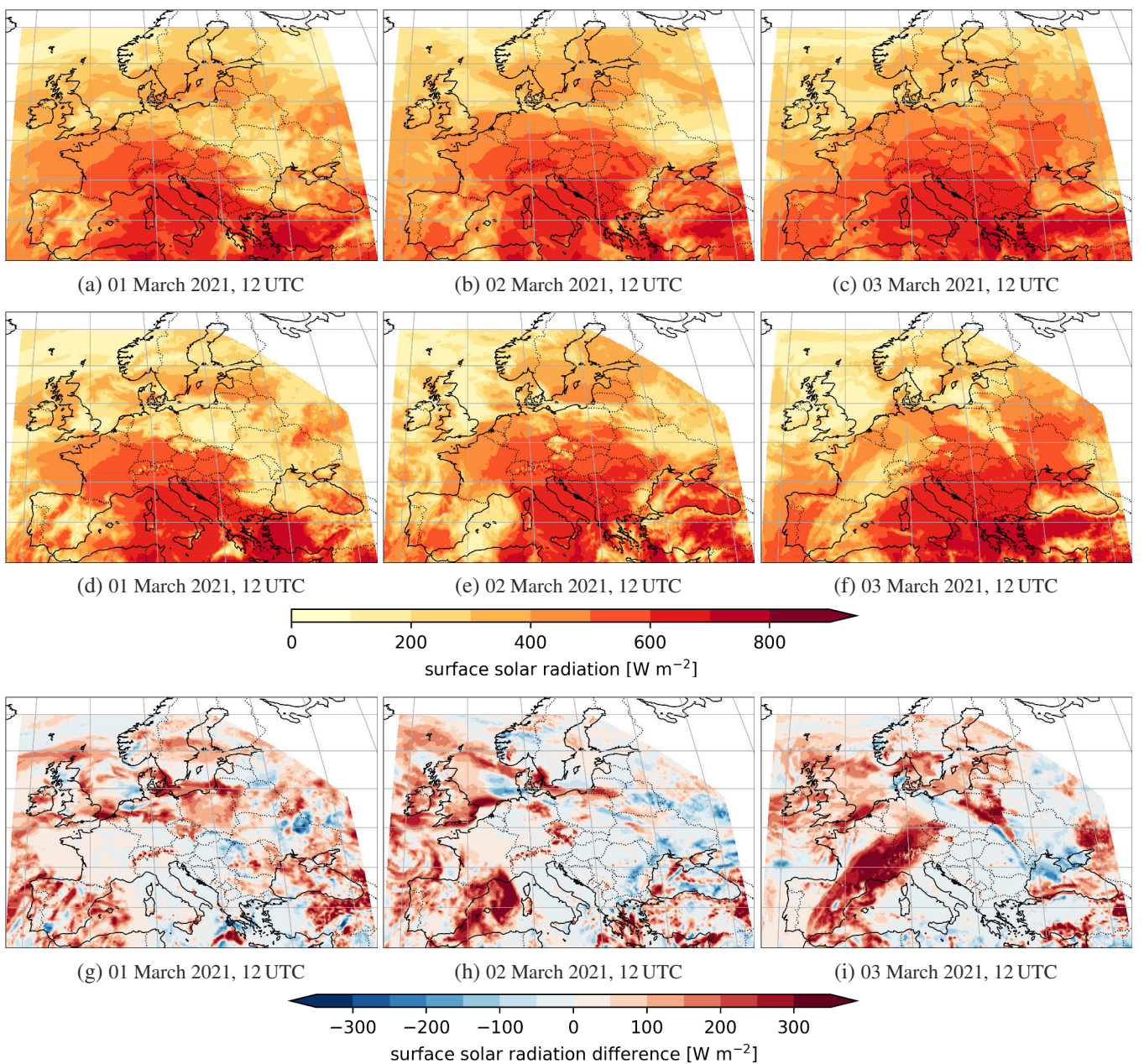


Figure 5.11: Overview about SIS from 01 to 03 March 2021. Simulated SIS in ECMWF IFS model (a–c), SIS derived from SEVIRI on Meteosat satellite (d–f) and difference between model and satellite values (g–i).

## 5.4 Comparison to Radiosonde Data

The previous sections show that disagreements in cloudiness between the CALIPSO retrieval and ICON-ART model data align with layers of high DOD. This can be due to processes induced by mineral dust, which is not implemented into the model, but also due to model errors in other quantities independent from dust. As the availability of moisture is a general precondition for the formation of clouds, we analyze temperature and moisture profiles from the model to examine whether errors in these quantities might cause the cloud errors. For this we compare simulated temperature and dewpoint profiles from the ICON-ART model to measurement data from radiosoundings. Figure 5.12 shows measured temperature and dew-point profiles from radiosoundings at selected stations on 03 March 12 UTC, and the value range of ICON-ART model data from the six closest cells to the launch location of the radiosonde. All stations are located in Central respectively Western Europe and experience a similar synoptic situation. Two stations (Nîmes, Payerne) are located directly under, one station (Stuttgart) is located at the northeastern edge and one station (Bordeaux) is located just outside of the cirrus cloud layer. The station in Payerne is also located very close to the surface track of the CALIPSO overpass, where ICON-ART shows a largely underestimated cloud cover.

The general agreement between model data and radiosoundings is very good. For temperature the model data fits excellent with measurements, with measured values mostly within the min-max range of model values. Small deviations exist with underestimations of the surface inversion (Stuttgart, Payerne) and slight underestimations of the Tropopause height for stations below the cirrus cloud (Stuttgart, Nîmes, Payerne). For moisture the model data fits well with measurements, with measured values mostly within the min-max range of model values. Prominent deviations occur for Stuttgart, where mid and high troposphere moisture is underestimated by the model. For Bordeaux and Nîmes, moisture in the low stratosphere is underestimated. For Nîmes, moisture in the boundary layer is underestimated.

Taking into account the uncertainty about the exact location of measurement due to the balloon drift, the model shows very good agreement with measurement data. Prominent deviations in temperature can be observed only for tropopause height at stations under the cirrus cloud. This might indicate additional radiative cooling from the cirrus cloud which is not reproduced by the model. The temperature profiles in other altitudes shows no prominent deviations, hence no sign for largely over- or underestimated direct or semi-direct aerosol effects. No large deviations from measured moisture can be observed, with the exception of Stuttgart which shows reduced moisture in the model. Nîmes and Payerne, which are located directly under the cirrus cloud, show very favorable temperature and moisture conditions for cirrus formation in the high troposphere, and very low temperatures below  $-40^{\circ}\text{C}$  which should even enable homogeneous freezing.

We conclude that the model is generally capable of reproducing the temperature and moisture conditions which lead to the observed cirrus cloud layer. Consequentially, model errors in moisture cannot be the reason for the missing cirrus cloud layer. The measured moisture in the high troposphere, observed cirrus clouds and the high dust layer in model simulations show vertical overlap. As mineral dust is effective as INP, this provides strong a indication that the presence of dust in high layers favored the formation of the high cirrus cloud on 02 and 03 March 2021.

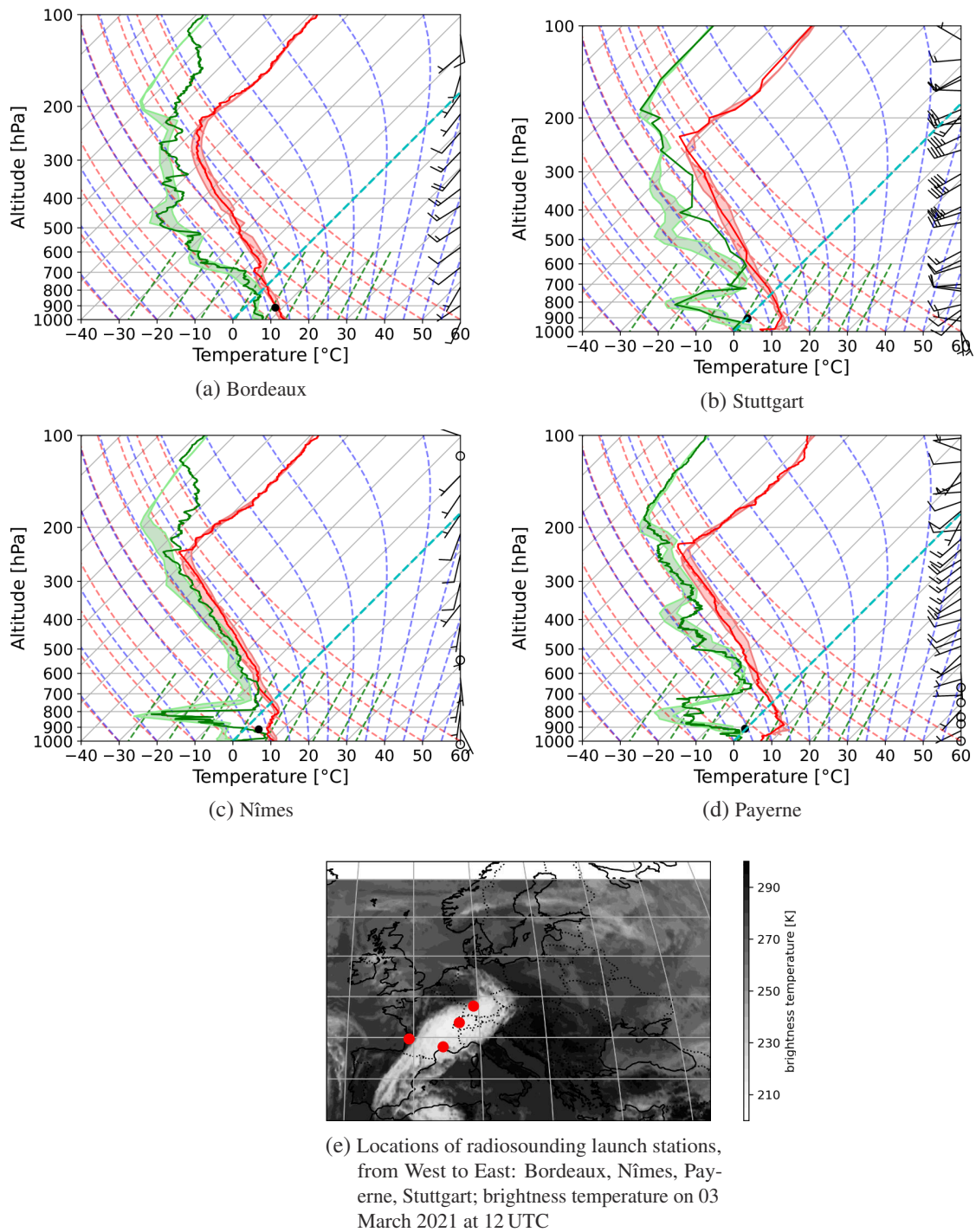


Figure 5.12: Radiosoundings for selected stations on 03 March 2021 at 12 UTC. Radiosounding data in solid lines, range of ICON-ART values from the closest 6 model cells to the radiosounding launch location as shaded area. Air temperature in red, dewpoint in green.

## 5.5 Comparison to Station Data

The previous sections analyze model data relative to satellite retrievals and radiosoundings. As satellite products can be biased, we compare SIS model data and satellite data to station data. We assume station data to be the most precise measure of the real world condition. Additionally we include model data from ICON versions with aerosol implementations of different complexity. We use a version with aerosol climatology (ICON) and a version with prognostic aerosol (ICON-ART) for examining whether the improved representation of direct aerosol effects improves forecast of SIS for the examined 03 March event. We perform analysis for the three selected stations Bonn, Rheinstetten and Hohenpeißenberg. Plots of SIS and DOD for these stations is shown in figure 5.13.

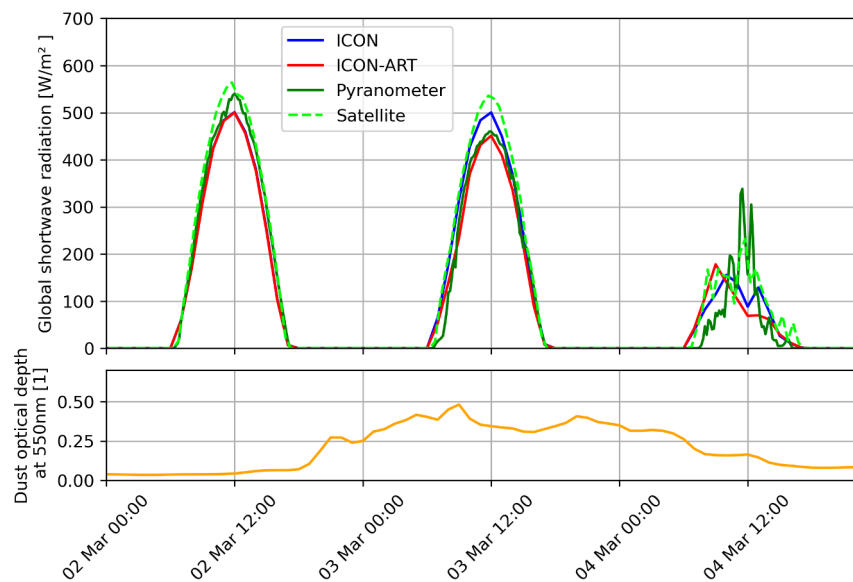
On 02 March, all stations are located under clear-sky conditions while DOD is low. SIS from pyranometer and satellite retrieval show very good agreement for all selected stations. Both ICON and ICON-ART show very similar values with and without aerosol effects, slightly underestimating SIS measured by the pyranometer and satellite.

On 03 March, all stations show increasingly dusty conditions and differing locations under the cirrus cloud. Bonn continues under clear-sky conditions, Rheinstetten is located at the northern edge of the cirrus cloud and Hohenpeißenberg is located under the cirrus cloud. For Bonn, the pyranometer shows reduced SIS compared to 02 March when DOD was low, suggesting the direct radiative effect from dust to cause this reduction. The satellite retrieval does not show strongly reduced SIS, providing an indication for a positive bias in SIS satellite retrieval during dusty conditions. This fits with the retrieval algorithm for SIS not using aerosol concentrations from recent measurements or model analysis but a prescribed aerosol climatology (Flentje et al. 2021, for more details see 3.2.1). Model data from ICON shows similar results, with SIS values on 03 March very close to 02 March. ICON does not reproduce reduced SIS during dusty conditions, hence overestimates SIS compared to the pyranometer. In contrast, ICON-ART clearly shows a reduction in SIS compared to 02 March and compared to ICON, with values which agree very well with the pyranometer measurement. This suggests the implementation of prognostic aerosol for the improvement of the direct radiative effect in ICON-ART to considerably improve radiation forecast during dusty clear-sky conditions. For Rheinstetten, the pyranometer shows strongly reduced SIS compared to 02 March and a very good agreement of pyranometer and satellite values. ICON and ICON-ART show similar behavior compared to Bonn, with ICON-ART showing a reduction of SIS due to the direct radiative effect from dust. Both model versions are largely underestimating the cirrus cloud cover and hence overestimate SIS throughout 03 March. For Hohenpeißenberg, the picture is similar to Rheinstetten but even more pronounced. Pyranometer and satellite values agree very well. The cirrus cloud shield leads to an overestimation of model SIS of about 50% for ICON-ART and 60% for ICON, suggesting that the current level of model complexity is not sufficient for adequately reproducing SIS during the examined dusty and cloudy conditions.

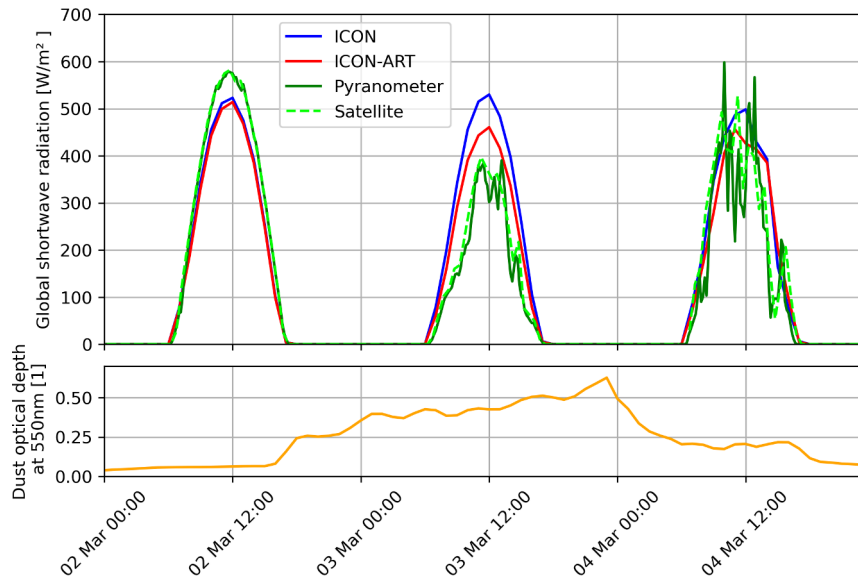
On 04 March, all stations experience changing conditions of cloudiness and reduced DOD compared to 03 March. Cloudiness on 04 March is mostly related to the cold front from a pronounced trough over Scandinavia. In contrast to 03 March, this frontal zone induced cloudiness is captured well

by the models. SIS from satellite retrieval agrees well with the pyranometer, only showing some smoothing which can be related to the lower time resolution of satellite SIS compared to the pyranometer. Models again show similar values and no clear difference between ICON without and ICON-ART with prognostic dust. Compared to measurement data, models show more smoothing at even lower time resolution, and possibly a slight overestimation for Rheinstetten and Bonn when integrating SIS over time. This however does not clearly indicate effects from the dust.

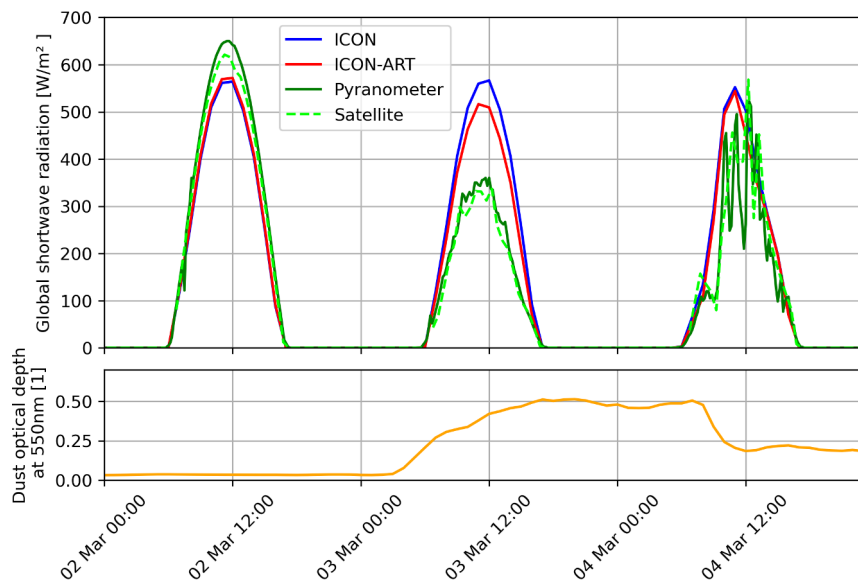
From intercomparison of SIS values from pyranometer, satellite and ICON versions with and without prognostic dust, several characteristic features can be summarized. Firstly, satellite retrievals generally match well with pyranometer measurements, especially during continuously cloudy conditions. Differences during dusty clear-sky conditions might be related to the use of an aerosol climatology in the satellite retrieval. For the statistical analysis of model errors, it must be considered that SIS from satellite retrievals might not be a reliable reference for the calculation of model errors during dusty clear-sky conditions. Secondly, model forecast during dusty clear-sky conditions improves with the inclusion of prognostic aerosol with direct radiative effects from dust. Thirdly, the forecast during dusty cloudy conditions is not captured well by either model, which suggests the implementation of prognostic aerosol with direct radiative effects not being sufficient for the model capturing cloudiness and subsequently SIS during these conditions.



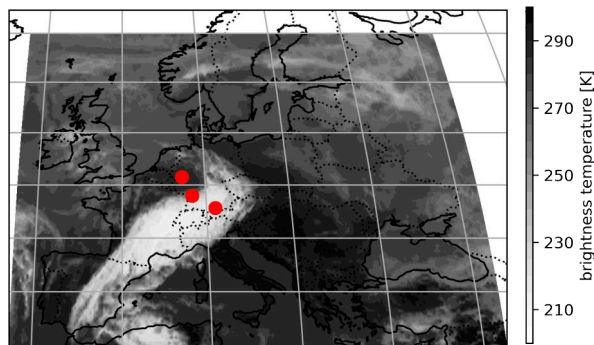
(a) Bonn



(b) Rheinstetten



(c) Hohenpeißenberg



(d) Locations of selected stations and brightness temperature on 03 March 2021 at 12 UTC

Figure 5.13: Intercomparison of SIS measurements and model data at selected stations with different cloudiness conditions on 03 March 2021: Bonn (clear-sky), Rheinstetten (at cloud edge) and Hohenpeißenberg (cloudy).

## 5.6 Summary of Case Study

This chapter shows that dust transport to Central Europe during the 03 March event happened in two vertical layers. A low-laying dust layer with a plume top height of about 5000 m reached Europe on 01 March and was advected with the general flow via the western Mediterranean towards France and the Benelux countries, and from there towards Germany. An elevated dust layer reached into altitudes of up to 11 km and became prominent on 02 March, presumably connected with effects from the short wave trough and upper low pressure zone over the British isles. The high dust layer above 5000 m showed a more direct transport of dust from the western Mediterranean over the Alps towards Central Europe.

Satellite data shows a high and spatially consistent cirrus layer in regions with dust in high atmospheric layers, which is not captured well by the models. Comparison of temperature and moisture profiles from the ICON-ART model, which includes the most complex implementation of aerosol processes among the examined models, to radiosoundings suggests the model capable of reproducing temperature and moisture conditions. Nevertheless, the prominent cirrus cloud on 02 and 03 March is consistently underestimated or missing in a model with prognostic calculation of aerosols (ICON-ART) and in models using aerosol climatologies (ICON, ECMWF IFS). The errors in cloudiness propagate into errors in SIS, reaching relative errors of up to 50% in the area of the underestimated cirrus cloud. The errors in cloudiness and SIS exist in both model forecast and analysis, suggesting a missing implementation of relevant processes in the model leading to this error. As the model errors in cloudiness align very well horizontally and vertically with the high dust layer above 5000 m, we conclude dust the most likely source for causing these errors. Furthermore the models with prognostic calculation of aerosol, which are examined in this study, only include the direct radiative effect of dust. As mineral dust can be efficient as INP, we conclude that the missing implementation of indirect aerosol effects is likely the cause of the models' failure in reproducing the cirrus cloud, especially in regions of high dust loading and otherwise favorable moisture conditions for the formation of cirrus clouds.

Comparison of model and satellite data to station data shows consistency of SIS satellite retrieval with pyranometer data during clear-sky conditions without dust, and during continuously cloudy conditions, where the optical depth from clouds dominates extinction in the atmosphere. During clear-sky conditions with dust, the satellite retrieval might not adequately capture SIS, as it does not take into account reduced SIS from increased direct radiative effects from dust. It should therefore be handled with caution when used as a reference. ICON and ICON-ART show improvements of the SIS forecast under dusty clear-sky conditions with the inclusion of prognostic aerosol with direct aerosol effect. Under cloudy conditions with dust, the direct aerosol effect is not sufficient for reproducing SIS from measurements, as models underestimate cloudiness.



## 6 Generalization: Dust Outbreak Synoptics and Forecasting Errors

In this section we analyze the typical synoptic conditions of dust outbreaks towards Central Europe and quantify model errors, with the aim of providing a robust and generalized statement about the characteristics and impacts of dust events. For this, we firstly perform a composite and cluster analysis of the synoptic situation during dust events. Secondly, we develop a methodology for the quantification of model errors during dust events. We then apply the newly developed methodology to data from the event catalog in order to quantify model errors in BT and SIS during the presence of mineral dust.

All model data in this chapter is from the ECMWF model family: Synoptic data is from ERA5, simulated BT from ECMWF IFS (hres), SIS from ECMWF IFS (ENS), DOD from CAMS. Satellite data for BT is from GridSat products, cloud mask and SIS is from MSG products. We only consider model analysis (BT, DOD) or short-range forecasts (SIS, forecast lead time of 3 h) in order to avoid errors resulting from synoptics. For a summary of data products used for this section, see table 6.1.

<b>Data source</b>	<b>Variable</b>	<b>Usage</b>
GridSat	brightness temperature	Reference for calculation of model error
Meteosat	cloud mask surface shortwave radiation	Reference for calculation of model error
Aeronet	coarse mode AOD	Validation of CAMS dust data
ECMWF IFS (operational)	brightness temperature surface shortwave radiation	Analysis of model error
CAMS (near-real-time)	integrated dust optical depth	Dust analysis for event selection, event catalog
ERA5 reanalysis	sea level pressure geopotential 10 m wind speed	Synoptic analysis for event catalog

Table 6.1: Summary of data products and variables used for the systematic synoptic analysis and generalization of dust events and forecasting errors.

## 6.1 Synoptic Analysis

Previous studies found that the advection of Saharan dust plumes towards the North Atlantic Ocean and the Mediterranean Sea can occur year-round (d'Almeida, 1986). At the same time the frequency of mineral dust events in the Mediterranean shows a pronounced seasonal behavior, which was found to be related to the cyclonic activity in North Africa (Moulin et al., 1998). Especially during spring, intense cyclones known as Sharav or Khamsin form under the influence of an upper level trough and conditions of strong baroclinicity between the North African coast and the Mediterranean. These cyclones travel eastwards along the North African coast (Alpert and Ziv, 1989), shifting the center of dust activity to the eastern Mediterranean. During Summer, the center of dust activity shifts westwards. Events are mostly connected to a pronounced trough near the Atlantic coasts of both Europe and Africa and a subtropical high pressure zone located further east over the Mediterranean or north Africa, which leads to a strong southwesterly flow (Moulin et al. 1998, Barkan et al. 2005). This seasonality affects the frequency of mineral dust events in the Mediterranean, which equally shows a pronounced seasonal behavior. Dust transport towards the eastern and central Mediterranean becomes prominent in spring, transport towards the western Mediterranean in early summer (Moulin et al., 1998). The number of dust events in western and southern Europe peaks in spring and summer months (Rodriguez et al. 2001, Escudero et al. 2005, Meloni et al. 2007).

In this section we analyze the typical synoptic situation during events with Saharan dust over Central Europe. We perform a cluster analysis for the investigation of different synoptic situations which lead to dust transport towards Central Europe and investigate seasonality in dust events over the same region. Finally we analyze typical dust emission regions and transport routes.

### 6.1.1 General Synoptic Situation

For assessing the general synoptic situation of Saharan dust events over Europe, we calculate composites from all events in the event catalog. The composite of 500 hPa geopotential, relative topography and mean sea level pressure in figure 6.1 shows a pronounced trough over the Iberian peninsula, which extends over the Atlas mountains and Algerian desert regions. This suggests dust pickup from the latter regions during increased wind speeds induced by frontal zone passages. With the tendency for quasi-geostrophic forcing ahead of the trough axis, dust can be lifted into higher atmospheric layers and quickly reaches Europe with the general flow. The composite from the complete event catalog also fits with the weather situation on 01 March, leading to the 03 March dust event which was examined in the case study, indicating this event to be representative for dust outbreaks towards Europe.

For assessing differences in the synoptic situations leading to dust events, we perform a cluster analysis. We use monthly averaged data from years 2018 – 2020 for removing the seasonal cycle from the 500 hPa geopotential for all individual events. The K-means clustering algorithm is then applied to the deseasonalized 500 hPa geopotential fields. Testing with different K-values,

partitioning into 2 clusters ( $k=2$ ) shows appropriate for our use. With  $k>2$ , additional clusters similar to the first cluster are classified (not shown). Composite plots for the general synoptic situation and DOD for the two clusters are shown in figure 6.2.

The composite plots show two synoptic situations leading to Saharan dust outbreaks towards Central Europe. Cluster one shows a pronounced omega situation over Europe, with a trough over the Iberian peninsula and northwestern Africa. Cluster two shows a similarly pronounced trough over the Iberian peninsula and northwestern Africa but higher pressure gradients are more zonally aligned isohypses over Central Europe, suggesting a stronger zonal flow and more variable weather compared to the omega situation in cluster one which tends to be more stationary and stable. Despite the two clusters showing differently pronounced geopotential fields, the general situation between the clusters is similar and favors dust transport from north Africa towards Europe.

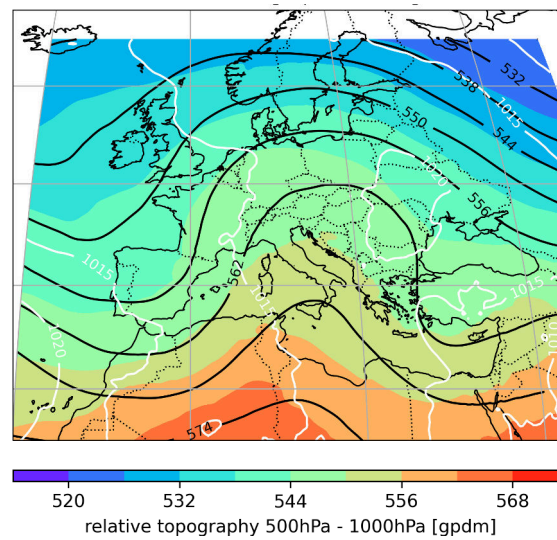


Figure 6.1: Synoptic composite of complete event catalog. 500 hPa geopotential (black contours), mean sea level pressure (white contours) and relative topography (filled contours).

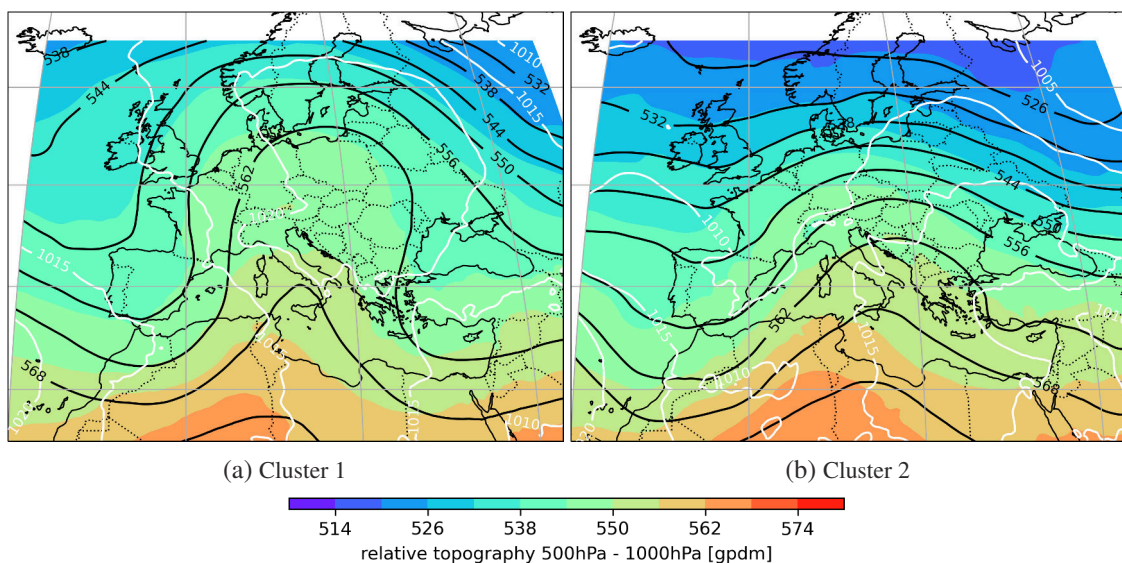


Figure 6.2: Synoptic composites from cluster analysis per cluster. 500 hPa geopotential (black contours), mean sea level pressure (white contours) and relative topography (filled contours).

### 6.1.2 Seasonality of Dust Outbreaks

Cluster analysis as outlined in the previous section yields two similar weather situations with differently pronounced flows. For synoptic purposes, we are interested if there are seasonal tendencies in the clusters. For this purpose, the monthly distribution of clustered events is summarized in table 6.2. This shows a general seasonality of dust events mostly to occur between late-winter until early-summer months, but does not show a distinct difference in seasonality between clusters. Due to the small number of 21 events, the robustness of any further seasonality examinations can be questioned. We conclude that the event catalog shows a tendency for dust events to occur between late-winter until early-summer months. This fits with Israelevich et al. (2012), who found dust events to occur predominantly occur over Central Europe during spring and summer months. In our study, the small number of events in the event catalog limits robust analysis of seasonality between the clusters.

Month	Cluster 1	Cluster 2
January	1	0
February	1	2
March	1	0
April	3	1
Mai	1	2
June	3	1
July	1	0
August	0	1
September	0	0
October	1	0
November	1	0
December	0	1

Table 6.2: Number of dust events between 2018 and mid 2021 per cluster and month.

### 6.1.3 Dust Emission Regions and Transport

Properties of dust and its interactions in the atmosphere are dependent on various factors such as its chemical composition, which is correlated to its emission region via the emitted mineral species or its residence time in the atmosphere and exposition to aging (Baker et al., 2014). For assessing possible differences in dust transport paths and source regions during the different synoptic situations found in section 6.1.1, we compute composites of DOD for the clustered events, which are shown in figure 6.3. From the 500 hPa geopotential fields we identify similar dust transport routes via the western Mediterranean towards Central Europe for both clusters. With the weaker pronounced westerly flow, cluster one suggests transport to Central Europe via central France. With the stronger pronounced westerly flow, cluster two suggests a more direct transport over the Alps. The DOD composites confirm this general pattern of dust transport via the western Mediterranean. DOD patterns between the two clusters however show only weak differences, but a tendency for

more dust over France for cluster one and a more direct transport to Central Europe for cluster two. Peak values over the restricted area are over France. The examination of individual events (not shown) shows large differences in the extend of the dust plume over Central Europe. While dust is typically advected via France, and hence consistently shows high DOD values over that region in the composite plots, dust only irregularly reaches the rest of Central Europe hence is averaged out for most regions such as Germany. Concluding, we cannot find distinctly different transport paths for the two clusters, however comparing DOD to the geopotential field suggests a tendency for transport towards Central Europe around the Alps for cluster one and over the Alps for cluster two.

For investigating dust source regions we discussed several approaches: Firstly, backward trajectories from the recorded dust plume over Europe and secondly, cluster analysis of conditions which can lead to dust emissions. Since seasonality analysis in the previous section did not provide clear results, we limit analysis to the simpler clustering approach. We use 10 m wind speed with a time-lag of 24 h before the dust event as a proxy for dust emission regions and calculate composites for the previously clustered events. This is shown in figure 6.4. Focusing on the upstream regions for Central Europe, weakly pronounced differences in the pattern of 10 m wind speed can be seen, with most prominent differences over the western Mediterranean Sea, but only weak differences over the Atlas mountains and Algerian desert regions. Comparison of the cluster composites for broader area of Europe and the Mediterranean suggests this magnitude of differences possibly being accidental or noise. Manual investigation of the individual events shows large spatial variations in peak wind speed patterns and varying time-lags in peak wind speeds before the recording of a dust event over Central Europe. This also applies for events from the same cluster. The high variability between events suggests the weak patterns in terms of 10 m wind speed to be non robust respectively the number of events being to small for results which can be distinguished from noise. We hence conclude that cluster analysis of 10 m wind speed cannot provide information about source regions of dust or distinct differences between the clusters.

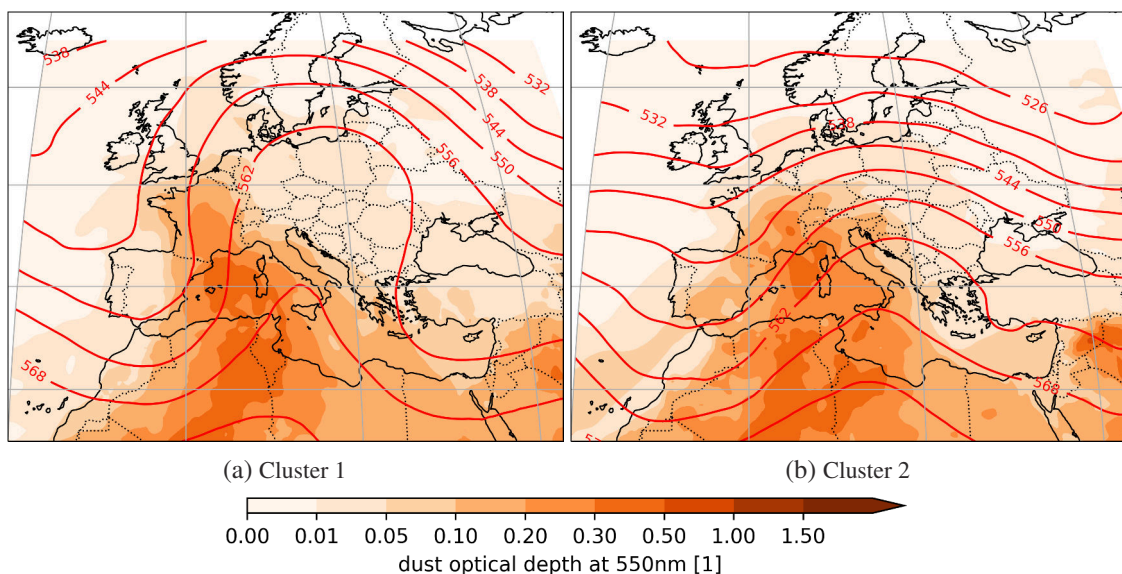


Figure 6.3: Synoptic composites from cluster analysis. 500 hPa geopotential (red contours) and vertically integrated DOD.

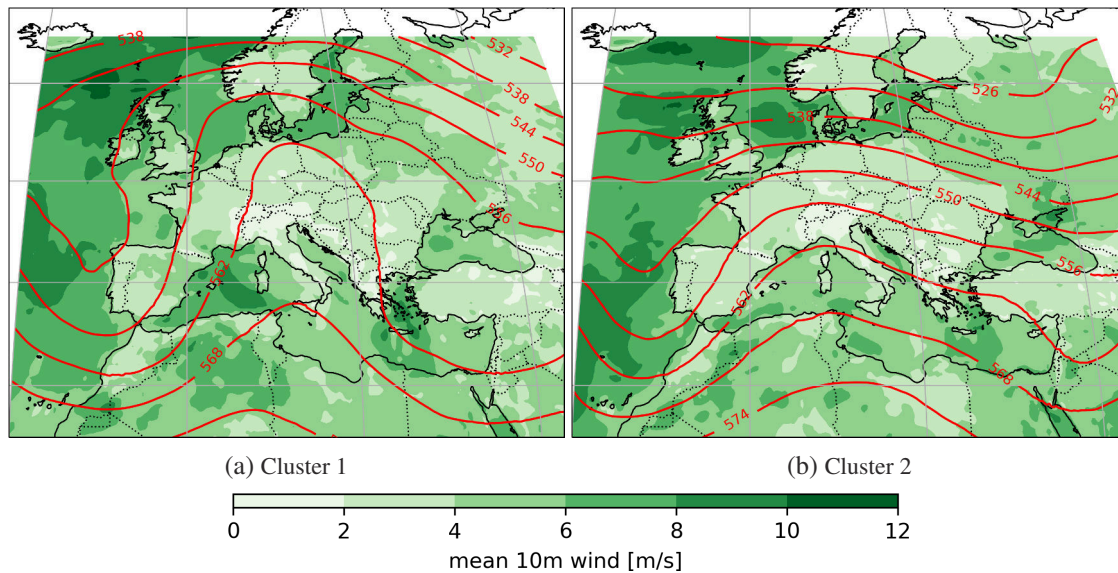


Figure 6.4: Synoptic composites from cluster analysis. 500 hPa geopotential (red contours) and 6 h mean 10 m wind speed. All values from 24 h prior to the dust events over Central Europe.

## 6.2 Quantitative Analysis

Previous studies found improvements of weather forecasts during individual dust events over Central Europe by including prognostic calculation of aerosol effects into models. This is quantified via improved forecasts of SIS or surface temperature (Rieger et al. 2015, Weger et al. 2018, Magnusson et al. 2021). Conversely, current operational weather forecasting models show errors during such dust events, as investigated in the case study in chapter 5. In this section we aim on generalizing model errors during events of Saharan dust over Central Europe. For this we use data from the previously defined event catalog and quantify median model errors in BT and SIS for dust events within the period 2018 to mid 2021.

### 6.2.1 Methodology and Case Classification

For the quantification of model errors during dust events, reference data is required. This can be an analysis or control run without the examined errors, or observation data, both serving as an estimate for the actual real world condition. We discussed several methods for being used within this thesis. Firstly, using model analysis data which is assumed to adequately represent the real condition, and comparing this to model forecast data with errors. At the time of this thesis project, the ECMWF operational analysis does not reliably reproduce the cirrus cloud cover during dusty conditions (e.g. on 03 March 2021, as discussed in chapter 5), hence this approach is not applicable. Secondly, comparing weather analogs without the observed cause of errors (in this case without a dust outbreak towards Central Europe) to the events with dust. Limited temporal availability of satellite products and inconsistent retrieval algorithms over time can become sources of uncertainties and/or limit the number of analog weather situations which can be used. Thirdly, comparison of satellite data as measurement of the real world condition against the model forecast.

With this method, an additional differentiation between errors from dust and systematic errors between model and satellite is advised. We achieve this by classification of model cells into cells affected by the hypothesized source of model error (dust) and without the hypothesized source of model error (no dust).

Since operational model analysis data shows errors for the most prominent dust events in March 2021, limited consistency of SIS satellite data for dates before 2018 limits the number of events which can be used as weather analogs, but a wide range of data is already available from the prior qualitative analysis, we choose the latter approach.

We classify all model cells by two criteria: Firstly, by the presence of dust we which we determine via the total DOD from the CAMS model (see section 3.1.2). Secondly, by cloudiness which we derive via TCC from the ECMWF IFS model (see section 3.1.1) and the MSG cloud mask (see section 3.2.1). To each model cell we apply both criteria for enabling differentiation between direct effects of dust during clear-sky conditions and indirect effects during cloudy conditions. This results in 4 specific cases: 1. clear-sky with dust, 2. clear-sky without dust, 3. cloudy with dust, 4. cloudy without dust. For the selection of threshold values for case classification, we perform a sensitivity analysis (see the following section 6.2.2).

In a subsequent step we calculate the model error for each cell, which we define as:

$$BT \text{ difference} = BT_{\text{model}} - BT_{\text{satellite}}$$

$$SIS \text{ ratio} = \frac{SIS_{\text{model}}}{SIS_{\text{satellite}}}$$

Using all cells within the respective case, we calculate statistics for the quantification of model error versus satellite data and for intercomparison between the four cases.

We further limit our analysis to the restricted area described in section 4.2. With this we focus on the area in Central Europe where the case study showed large model errors during the examined dust event. This also limits analysis to values over land and avoids possible satellite biases between land and sea surfaces, while keeping a large number of cells for classification into the four cases. Finally the selected area contains Germany, Baden-Württemberg for which the previously shown errors in PV forecast were recorded.

### 6.2.2 Threshold Sensitivity Analysis

For the selection of threshold values for classification into the four cases clear-sky with dust, clear-sky without dust, cloudy with dust, cloudy without dust, we perform a sensitivity analysis of BT and SIS errors to cloudiness and dust thresholds. For this, one criterion threshold is kept constant at a pre-selected value and the other criterion threshold is modified. For the dust criterion, we pre-select a single threshold for the division into a dust and a no dust case as a DOD of 0.1. This consistent with earlier studies using an AOD threshold of 0.1 for differentiation from background aerosol (Holben et al., 1998). For the cloudiness criterion from model data we pre-select an upper

limit for clear-sky classification as TCC of less than 25% and a lower limit for cloudy classification as a TCC of greater than 75%.

Figure 6.5a,c shows sensitivity analysis of BT and SIS to the dust criterion. It shows varying sensitivity of the different cases to the variation of the DOD threshold value. The general trend shows an increase of model error in BT with increasing DOD threshold, but only the case *cloudy with dust* (red solid) shows a strong increase of model errors with increasing DOD. Also for SIS, only the case *cloudy with dust* shows a strong increase of model errors with increasing DOD. For both BT and SIS, this case shows a prominent increase in model error around the pre-selected DOD threshold of 0.1, increasing further with increasing DOD values. Around a DOD of 0.4 the curves begin to flatten or even decline, suggesting stabilization of maximum errors around this threshold. For the other cases, the increase in model errors between DOD values of 0.1 and 0.4 is small. For very high threshold values, the area represented by the selected cells drops to zero or very low values for the two cases with dust. Hence the decrease of model errors for very high DOD values is presumably not robust and might be attributed to the very small sample size.

Figure 6.5b,d shows sensitivity analysis of BT and SIS to the cloudiness criterion. It shows low sensitivity for the variation of cloud fraction limits towards low as well as high values. The area represented by the selected cells remains large and of similar magnitude through the tested range of 1 to 99% TCC, hence we keep the pre-selected limits of 25% respectively 75% TCC. This includes a large number of cells into analysis, and also considers the cases where not only cloud height or thickness but also TCC was slightly over- or underestimated in the model, while ensuring a clear distinction between cloudiness conditions within the cases. We subsequently compare the so derived cloudiness classification to the MSG cloud mask and only keep cells with the same cloudiness class from model and satellite data. The following table 6.3 shows a summary of the decision criteria and cases.

		Dust threshold	
		DOD $\geq$ 0.1	DOD $<$ 0.1
<b>Cloudiness threshold</b>	TCC $>$ 75%	cloudy, dust	cloudy, no dust
	MSG: cloud		
<b>&amp;</b>	TCC $<$ 25%	clear-sky, dust	clear-sky, no dust
	MSG: clear-sky		

Table 6.3: Decision criteria and selected thresholds for the classification of model cells into four cases.

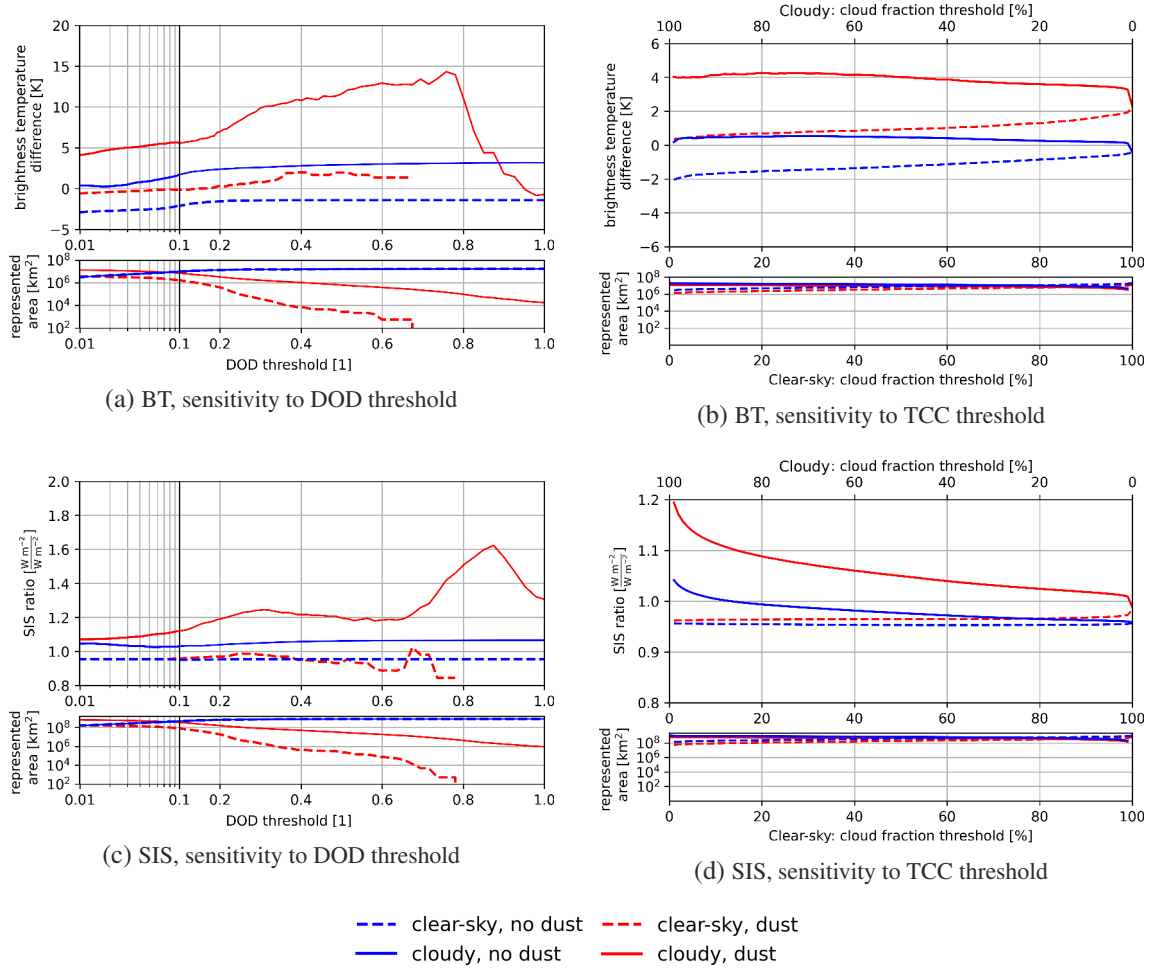


Figure 6.5: Sensitivity to classification thresholds for BT and SIS, and area represented by the specific case. Threshold values for the fixed decision criteria are TCC of 25% or 75% and DOD of 0.1.

### 6.2.3 Quantitative Results

For the quantification of dust effects on model errors, we sort all model cells into the four cases as outlined in the previous section. We select threshold values for the cloudiness criterion of 25% respectively 75% TCC and threshold values for the dust criterion of 0.1 and 0.4 DOD. We then calculate model errors from satellite data for each cell in the respective case and analyze the resulting distributions, which are shown in figure 6.6.

Comparing absolute model errors, prominent differences between the cases stand out. Firstly, the cloudy cases show a wide distribution of model errors (figure 6.6a–d, solid boxes), compared to a narrow distribution for clear-sky cases (figure 6.6a–d, dashed boxes). As this persists in both cases with dust and without dust, we connect the broad error distribution in the cloudy cases to non-dust-related temporal and spatial shifts in cloudiness between model and satellite, an error which is also observed within the case study. The narrow distribution of clear-sky errors suggests consistency of model results compared to satellite retrievals. Secondly, the case *cloudy with dust* shows the largest median model error for both BT (5.6 K and 11.0 K, figure 6.6a–b, red solid) and SIS (12% and 22%, figure 6.6c–d, red solid) at both DOD thresholds (0.1 and 0.4). Median model errors are smaller for the other cases and of similar magnitude between cases. This suggests the

*cloudy with dust* case to be the most prominent source of model errors for these two variables. Thirdly, median errors for clear-sky cases are negative (figure 6.6a–d, dashed), which might indicate that the model underestimates BT and SIS for those cases. Only the *clear-sky with dust* case for BT and a DOD of 0.4 (figure 6.6d, red dashed) deviates from this pattern. The represented area from this case is very small, hence the robustness of the value can be called in question. Furthermore, the SIS errors for clear-sky cases with dust should be handled with extreme care, as the satellite data used as reference shows indications for a bias during these conditions. The underestimation of BT and SIS for clear-sky cases without dust is small but consistent between variables and dust thresholds, which might be attributed to a general bias in model or satellite data.

Setting median errors for cases with dust in relation to the cases without dust, information about the effect of dust can be drawn. We test significance of the differences in the medians between the case with dust and corresponding case without dust via bootstrapping the difference of medians. We draw samples from both cases with a length equal to the sample size of the smaller case, and calculate the difference in sample medians for each bootstrap replicate. We use a total number of 1000 bootstrap replicates for calculating the bootstrapping distribution. For all tests, we select a 95% confidence interval around the bootstrapping distribution median and call the differences significant where this interval does not extend over zero.

For clear-sky cases, the differences in BT median errors between the cases with dust and without dust reach about 1.9 K (3.4 K) for a DOD threshold of 0.1 (0.4) and are significant. For SIS, the differences in median errors between the cases with dust and without dust are very small and bootstrapping the difference of medians does not show significance. This might suggest that the direct aerosol effect plays only a minor role for causing the model errors during the events in the event catalog. This however is not consistent with the findings in section 5.5, which shows clear indications for the direct aerosol effect causing model errors during clear-sky conditions in models without prognostic aerosol. As especially the SIS satellite product shows indications for a positive bias during clear-sky conditions, we conclude that for the clear-sky cases we can neither prove nor rule out a significant error from dust.

For the cloudy cases, the differences in BT median errors between the cases with dust and without dust are much higher than for clear-sky cases. Absolute differences in medians reach 2.9 K (9.2 K) for a DOD threshold of 0.1 (0.4) and are significant via the bootstrapping distribution. Absolute differences in SIS median errors reach 9% (15%) for a DOD threshold of 0.1 (0.4), which translates into relative differences of about 15% for both DOD thresholds. The differences are significant via the the bootstrapping distribution. The error in cloud properties hence leads to errors in SIS, with a relative median model error in SIS of about 15% between cloudy conditions with and without dust for both DOD thresholds of 0.1 and 0.4. This shows dust playing a major role for causing model errors during cloudy conditions, when the presence of dust leads to an underestimated cloudiness, cloud depth or cloud top height.

In summary we do not find clear results about the magnitude and significance of model errors during clear-sky conditions. There are indications for small but significant errors in BT (in this case a proxy for radiative effects from dust). However we do not find robust results about effects on SIS, as the SIS satellite product shows indications for a bias during clear-sky conditions with dust

(see section 5.5. This bias is known and due to the deployment of a dust climatology within the retrieval algorithm (EUMETSAT, 2021b). For cloudy conditions, we find major model errors in BT, affecting SIS and causing median SIS errors of about 15% during dust events relative to events without dust. Model errors during dust events increase with increasing DOD. We conclude that at least for cloudy conditions, dust shows a significant impact on forecast quality.

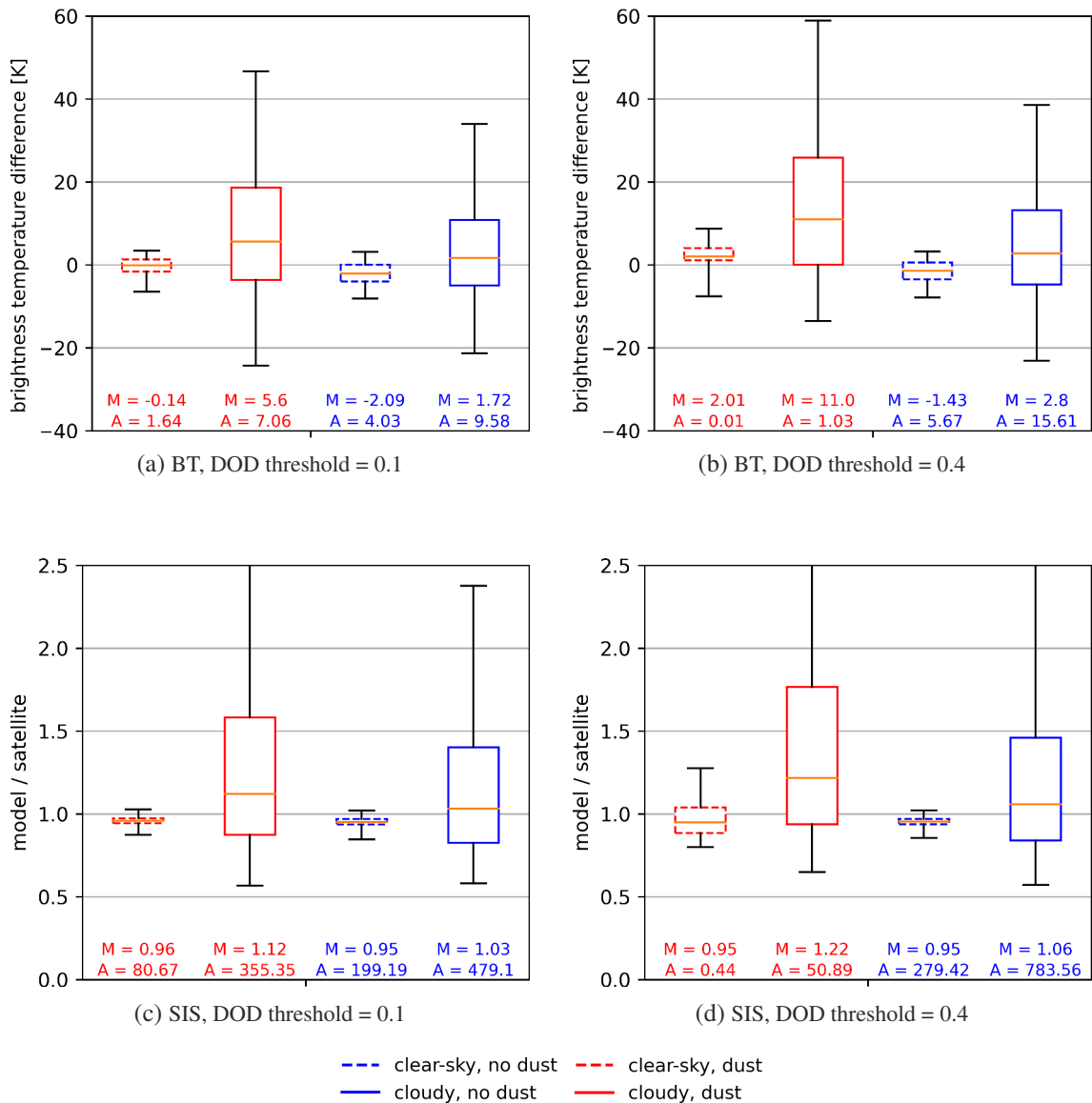


Figure 6.6: Boxplots for model errors in BT and SIS relative to satellite data for the four cases. Orange lines represent the median value, box outlines the 25th and 75th percentile, whiskers the 5th and 95th percentile. Median of respective box (M) and represented area (A) are given numerically.

### 6.3 Cases with Inverse Cloudiness in Model and Satellite

The previous quantitative analysis focused on cases where both model and satellite classify the same cloudiness case (both clear-sky or both cloudy). Consequentially, errors between model and satellite result from, e.g. underestimation of cloud height, cloud thickness or cloud brightness but only partially from cloud fraction. The case study however shows that in some cases the model does not reproduce cloudiness at all. For assessing the cases where the MSG cloud mask classifies *cloud* and the model *clear-sky* (and reverse), we calculate the relative frequency of such inverse cloudiness classification within all cases with dust and all cases without dust. For obtaining a measure for the sensitivity of such cases to DOD, we apply the same threshold variation as in section 6.2.2. This is shown in figure 6.7.

For DOD thresholds below 0.1, the relative frequency of inverse cloudiness classification is similar among all cases and in the range of 5 to 7% of total cases, with the number of values (the number of model cells where this occurs) in the same magnitude for all cases. For increasing DOD, the cases with dust show a pronounced pattern. The relative frequency of cases with clouds in the satellite cloud-mask but clear-sky in the model increases sharply by about 50% between DODs of 0.1 and 0.2, to 9% of total cases with dust (red solid). The relative frequency of the reverse case (red dashed) decreases with increasing DOD. This pattern suggests that for cases with dust the model frequently underestimates but rarely overestimates cloud cover compared to the MSG cloud-mask. This especially occurs for DODs above 0.1 and fits with findings from the case study of 03 March 2021 (see chapter 5), confirming that the model does not reproduce cloudiness in some cases with high loads of dust. For higher DODs the number of cases with dust strongly decreases and the relative frequency of cases should not be assumed as robust. The cases without dust (blue dashed and solid) only show a weak sensitivity to DOD. Comparing the cases without dust to the cases with dust, and including the findings from the case study that underestimation of cloudiness especially occurs during the presence of dust, we conclude that dust is the likely cause of frequent underestimation of cloud fraction within the event catalog.

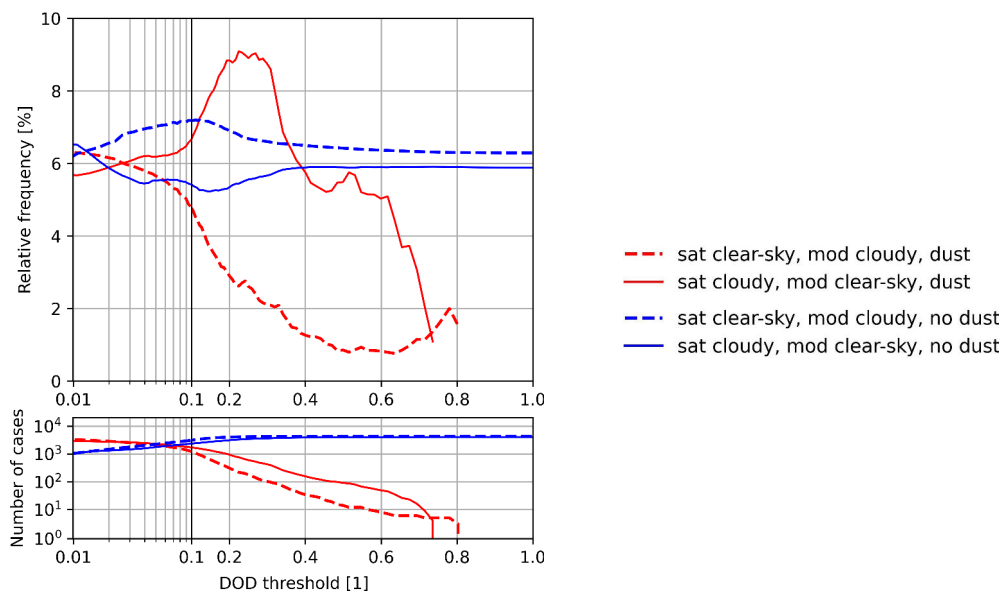


Figure 6.7: Frequency of inverse cloudiness classification between MSG cloud mask and model threshold criterion. Threshold values for clear-sky and cloudy from model data are TCC of 25% and 75%.

## 6.4 Summary of Generalization

This chapter shows that dust events in Central Europe originate from two similar but differently pronounced synoptic situations. The most common situation is a pronounced trough over the Iberian peninsula and northwestern Africa with an omega situation over Central Europe. The second situation equally shows a trough over the Iberian peninsula and northwestern Africa, but a more zonal flow over Central Europe. The distribution of dust events throughout the year shows a seasonality with peak between late-winter until early-summer. This is consistent with previous studies which found dust activity in the western Mediterranean to increase towards summer (Rodríguez et al. 2001, Escudero et al. 2005, Meloni et al. 2007), and the highest activity over Central Europe during early summer (Israelevich et al., 2012). We do not find clear seasonality differences between the two synoptic clusters, nor clearly different source regions of dust. The transport patterns however show a weak tendency for dust transport to Germany via France and the Benelux countries for the omega situation and a more direct transport to Germany via the Alps for the situation with more zonal flow.

For quantitative analysis we classify model cells into four different cases with clouds or clear-sky and dust or no dust. This assesses errors during conditions where both model and satellite show similar cloud fraction. Analysis of the classification thresholds shows a strong sensitivity for the case *cloudy with dust* in BT and SIS errors to the variation of the DOD threshold in the range 0.1–0.4. For higher DOD values, a flattening or decrease of the curve suggests extremely high dust loads not leading to higher errors in cloudiness, which can be an indication for a saturation of temperature and moisture conditions to CCN respectively INP activation. For other cases the sensitivity to the DOD threshold is low, so is the sensitivity to cloudiness threshold.

The quantification of model errors shows absolute errors largest for the case *cloudy with dust* for both BT (5.6 K and 11.0 K) and SIS (12% and 22%) at both DOD thresholds (0.1 and 0.4), which suggests this case the most prominent source of model errors concerning the two variables considered. Median errors between the cases with dust and without dust are most prominent for cloudy conditions and reach 2.9 K (9.2 K) for BT and 9% (15%) for SIS at a DOD threshold of 0.1 (0.4). Differences in medians between the cloudy cases with dust and without dust are significant at a 95% confidence level. For clear-sky conditions the differences are much smaller. The satellite retrieval of SIS shows indications for a positive bias during clear-sky conditions with dust, as the retrieval algorithm deploys an aerosol climatology. Hence we cannot draw reliable conclusions about SIS under clear-sky conditions.

Examination of the cases where model and satellite show different cloud fraction shows increasingly frequent underestimation of cloud fraction for DOD greater 0.1, which fits with the findings from the case study.

Concluding, absolute model errors relative to satellite, and relative errors of the dust case to the no dust case suggest misrepresentation of cloudiness to play the dominant role for causing model errors during dust events. The finding of increased TCC underestimation during dust cases underlines this. This means that we find indications for both underestimations in cloud optical depth, height or brightness (section 6.2) and TCC (section 6.2.3), which emphasizes the need for the inclusion of the indirect effect into NWP models in order to improve the representation of cloud properties.



## 7 Discussion and Conclusion

Every year several events with transport of Saharan dust towards Central Europe occur (d'Almeida, 1986), which affects air quality and weather via aerosol-radiation-cloud interactions. Models which are currently used for operational weather forecasting cannot reproduce these effects as they rely on climatologies (e.g. ECMWF 2021a, Reinert et al. 2021). Even models with prognostic calculation of aerosols and dust often do not include effects of dust on clouds and radiation (e.g. Flentje et al. 2021). This can lead to large errors in weather forecasting during dust events (Magnusson et al., 2021) and disturbs services such as PV power generation forecast, which rely on correct SIS forecast (see chapter 1, Köhler et al. 2017). This thesis investigates the source of model errors during dust events and aims on providing a generalized quantification of the effect of dust on weather forecast over Europe.

We perform a case study for a selected dust event on 03 March 2021 and examine the skill of current models to reproduce the observed and measured weather conditions (chapter 5). In a next step we investigate the general synoptic situation which leads to dust outbreaks towards Central Europe (chapter 6, section 6.1). We then perform a quantification of model errors versus satellite data and test the significance of error differences between cases with dust and cases without dust (chapter 6, section 6.2). In this section we first answer the central research questions as outlined in chapter 1. We then discuss the implications of our findings and suggest directions for future research.

The main research questions can be answered as follows:

- 1. What is the cause for the prominent model errors during the dust events in spring 2021? Is dust related to the model errors or are other processes or quantities causing the errors?**

We examine the dust event on 03 March 2021 as a representative case for the dust events during spring 2021. Different models (ECMWF IFS, ICON, ICON-ART) show largely underestimated cirrus cloud cover, which leads to largely underestimated SIS. Model errors show very good spatial (horizontal and vertical) alignment with mineral dust. Vertical temperature and moisture profiles from the ICON-ART model excellently agree with radiosonde measurements. SIS during conditions without dust, agrees well between model data, satellite retrievals and station measurements. Only one model (ICON-ART) calculates dust prognostically, and no model performs prognostic calculation of indirect (dust) aerosol effects. We conclude that the lacking implementation of dust indirect effect is most likely the reason of the model errors.

## 2. What is the general synoptic situation leading to dust events over Central Europe?

The typical synoptic situation leading to dust events over Central Europe shows a pronounced trough extending over the Iberian peninsula towards northwestern Africa, and a high pressure zone over Central Europe. For the events between 2018 and mid 2021 this is most frequently an omega-like situation with the high pressure center over Central Europe, followed by a situation with a weakly pronounced ridge over Central Europe. Both events lead to a southwesterly flow over the western Mediterranean, with which dust is transported towards Central Europe. The omega situation shows a weak tendency for dust transport to Germany via France and the Benelux countries. The situation with the weakly pronounced ridge shows a more direct transport path to Germany via the Alps. Dust events with these synoptic situations occur year-round but show highest frequency between late-winter until early-summer months.

## 3. How can model errors during dust events be quantified? How large are the typical errors during dust events over Central Europe?

We use analysis and forecast data from the ECMWF IFS model and assess BT as proxy for cloud properties, and SIS as an indication for error propagation into further meteorological quantities. We quantify model errors by comparison against satellite data. For events with similar TCC in model and satellite, we classify model cells into four cases: clear-sky with and without dust, and cloudy with and without dust. Absolute errors are highest for cloudy conditions with dust, with median absolute errors in BT of 5.6 K (11.0 K) and median absolute errors in SIS of 12% (22%) for dust cases with DOD greater than 0.1 (for extreme dust cases with DOD greater than 0.4). Differences between the cases with and without dust are highest for cloudy conditions, with differences in median errors in BT of 2.9 K (9.2 K) and differences in median errors in SIS of 9% (15%) for dust cases with DOD greater than 0.1 (for extreme dust cases with DOD greater than 0.4). These differences are significant at a 95% confidence level and indicate a significant effect of dust on cloud properties such as cloud depth, cloud height or cloud brightness, as well as on SIS. For clear-sky cases, absolute errors in BT are much smaller than for cloudy conditions. Differences between the cases with and without dust in BT reach 1.9 K (3.4 K) for dust cases with DOD greater than 0.1 (for extreme dust cases with DOD greater than 0.4). Differences are significant at a 95% confidence level and suggest underestimation of a direct radiative effect from dust. Quantification of clear-sky SIS against satellite data is unreliable, as the satellite retrieval is biased under clear-sky conditions with dust. Furthermore we analyze events where the model does not reproduce cloud cover. We find indications for increasingly frequent underestimating but rarely overestimation of TCC for cases with DOD greater than 0.1. In summary, we find indications for both underestimations in cloud optical depth, height or brightness and TCC during dust events.

In the following we briefly discuss agreement of these main findings with literature and outline implications for future research and model developments.

---

The case study of 03 March 2021 in chapter 5 shows that operational weather forecasting models in 2021 still lack the skill to adequately reproduce cloudiness during dust events. NWP models which are currently used for operational weather forecasting (ECMWF IFS, ICON) generally do not reproduce increased dust concentrations during Saharan dust outbreaks towards Europe, as dust concentrations are prescribed via climatological means. This leads to model errors via underestimation of direct and indirect effects of dust. We find that the implementation of prognostic aerosol and direct radiative effects improves SIS forecast under clear-sky conditions, compared to models which use aerosol climatologies. Models with prognostic calculation of mineral dust (ICON-ART) include direct radiative effects from dust, but often do not include indirect aerosol effects in their currently operational versions. Previous case studies have shown that models with prognostic aerosol and direct effect, but without prognostic indirect effects tend to underestimate cloud ice and high cloud cover during dust events. The inclusion of indirect dust effects can lead to increased glaciation of clouds and a better representation of cirrus clouds during dust events (Weger et al., 2018). Further studies have shown that the prognostic calculation of dust can improve SIS forecast (Rieger et al., 2017) and 2 m temperature forecast (Magnusson et al., 2021) during dust events. With the observed model errors mostly resulting from underestimated cirrus cloud cover, temperature and moisture being reproduced well by the model with most complex implementation of dust effects, and mineral dust being efficient as CCN and INP, the missing model implementation of indirect aerosol effects is likely the cause for these errors. Our study hence agrees with previous research and highlights the need of implementing aerosol indirect effects into the operational versions of coupled models in order to adequately reproduce cloudiness during Saharan dust events over Central Europe. Concerning services such as the forecast of PV power generation, the need for the implementation of prognostic aerosol also into operational weather forecasting models is apparent in order to improve these forecasts.

Analysis of the typical synoptic situation during dust events within the event catalog in chapter 6, section 6.1 shows two similar but differently pronounced situations. Both show a trough over the Iberian peninsula and a high pressure zone over Central Europe or the Central Mediterranean, which leads to a strong southwesterly flow and dust transport towards Central Europe via the western Mediterranean. This agrees with findings from previous studies (e.g. Barkan et al. 2005) and shows a similar seasonality with peaks between late-winter until early-summer months as found by Israelevich et al. (2012). We find only weak differences in dust transport paths between the two synoptic situations and cannot answer whether there are distinctly different source regions of dust. Chemical properties of dust are linked to the mineral species emitted from the particular source region, and dust is exposed to chemical reactions which also alter its properties during transport (Baker et al., 2014). Further systematic investigation of dust source regions and transport paths in future projects can provide information about the efficiency of dust for acting as CCN and INP under specific synoptic situations. Furthermore, recent studies find that extreme dust events with dust transport as far north as Central Europe coincide with the occurrence of atmospheric rivers (Francis et al., 2022), elongated narrow bands of clouds with high water vapor content (Newell et al., 1992). This implies that dust events often occur alongside events with high moisture transport towards Europe, which once more highlights the necessity of implementing prognostic calculation of indirect dust effects into models.

The systematic quantification of model errors in chapter 6, section 6.2 shows that model errors do not only occur during individual dust events but consistently cause model errors during conditions with high concentrations of mineral dust. With the applied methodology we are able to quantify these errors during cloudy conditions. During clear-sky conditions however we cannot complete the quantification of dust effects. Despite indications for a significant direct radiative effect of dust in BT, impacts on SIS cannot be quantified as the satellite product for SIS shows a bias during clear-sky conditions as it deploys an aerosol climatology within the retrieval algorithm (Pfeifroth and Trentmann, 2018). The SIS satellite product hence does not account for the increased direct radiative effect from dust during Saharan dust events over Europe. Previous studies suggest that forecast improvements with including prognostic aerosol are dominated by improvements in the representation of the direct radiative effect (Rieger et al., 2017). This implies that the direct radiative effect of dust actually plays an important role for causing forecast errors. It can therefore be worthwhile to investigate model errors during clear-sky conditions in a future project, for example by extending the systematic analysis of model errors to station measurements of SIS. Furthermore, the systematic analysis can be extended into further variables such as the 2 m temperature for examining error propagation into further meteorological quantities. Finally the model improvements with the implementation of indirect aerosol effects should be assessed as soon as model implementations of these processes are complete.

# Abbreviations

<b>AERONET</b>	Aerosol Robotic Network
<b>AOD</b>	Aerosol optical depth
<b>ART</b>	Aerosol and Reactive Trace gases
<b>BT</b>	Brightness temperature
<b>CALIOP</b>	Cloud-Aerosol Lidar with Orthogonal Polarization
<b>CALIPSO</b>	Cloud-Aerosol Lidar and Infrared Pathfinder Satellite Observations
<b>CAMS</b>	Copernicus Atmosphere Monitoring Service
<b>CCN</b>	Cloud condensation nuclei
<b>CDNC</b>	Cloud droplet number concentration
<b>DOD</b>	Dust optical depth
<b>DWD</b>	Deutscher Wetterdienst (German Weather Service)
<b>EBR</b>	Extinction to backscatter ratio
<b>ECMWF</b>	European Centre for Medium-Range Weather Forecasts
<b>GCN</b>	General circulation model
<b>ICON</b>	Icosahedral Nonhydrostatic
<b>IFS</b>	Integrated Forecasting System
<b>INP</b>	Ice nucleating particle
<b>MSG</b>	Meteosat Second Generation
<b>PV</b>	Photovoltaic
<b>SDA</b>	Spectral Deconvolution Algorithm
<b>SEVIRI</b>	Spinning Enhanced Visible and Infrared Instrument
<b>SIS</b>	Surface incoming shortwave radiation
<b>TCC</b>	Total cloud cover



# Bibliography

- Ackermann, I. J., H. Hass, M. Memmesheimer, A. Ebel, F. S. Binkowski, and U. Shankar, 1998: Modal aerosol dynamics model for Europe: Development and first applications. *Atmospheric environment*, **32** (17), 2981–2999.
- Albrecht, B. A., 1989: Aerosols, cloud microphysics, and fractional cloudiness. *Science*, **245** (4923), 1227–1230.
- Alpert, P., and B. Ziv, 1989: The Sharav cyclone: observations and some theoretical considerations. *Journal of Geophysical Research: Atmospheres*, **94**, 18 495–18 514.
- Aminou, D., 2002: MSG's SEVIRI instrument. *ESA Bulletin (0376-4265)*, (111), 15–17.
- Baker, A. R., O. Laskina, and V. H. Grassian, 2014: Processing and ageing in the atmosphere. *Mineral dust*, Springer, 75–92.
- Barkan, J., P. Alpert, H. Kutiel, and P. Kishcha, 2005: Synoptics of dust transportation days from Africa toward Italy and central Europe. *Journal of Geophysical Research: Atmospheres*, **110**.
- Beyer, H. G., C. Costanzo, and D. Heinemann, 1996: Modifications of the Heliosat procedure for irradiance estimates from satellite images. *Solar Energy*, **56** (3), 207–212.
- Boucher, O., and Coauthors, 2013: Clouds and aerosols. *Climate Change 2013: the physical science basis. Contribution of Working Group I to the Fifth Assessment Report of the Intergovernmental Panel on Climate Change*, Cambridge University Press, 571–657.
- Bozzo, A., S. Remy, A. Benedetti, J. Flemming, P. Bechtold, M. J. Rodwell, and J.-J. Morcrette, 2017: *Implementation of a CAMS-based aerosol climatology in the IFS*. European Centre for Medium-Range Weather Forecasts.
- Bristow, K. L., and G. S. Campbell, 1984: On the relationship between incoming solar radiation and daily maximum and minimum temperature. *Agricultural and forest meteorology*, **31** (2), 159–166.
- Carslaw, K., O. Boucher, D. Spracklen, G. Mann, J. Rae, S. Woodward, and M. Kulmala, 2010: A review of natural aerosol interactions and feedbacks within the Earth system. *Atmospheric Chemistry and Physics*, **10** (4), 1701–1737.
- Cziczo, D. J., and Coauthors, 2013: Clarifying the dominant sources and mechanisms of cirrus cloud formation. *Science*, **340** (6138), 1320–1324.

- d'Almeida, G. A., 1986: A model for saharan dust transport. *Journal of Applied Meteorology and Climatology*, **25** (7), 903–916.
- DeMott, P. J., K. Sassen, M. R. Poellot, D. Baumgardner, D. C. Rogers, S. D. Brooks, A. J. Prenni, and S. M. Kreidenweis, 2003: African dust aerosols as atmospheric ice nuclei. *Geophysical Research Letters*, **30** (14).
- Derrien, M., and H. Le Gléau, 2005: MSG/SEVIRI cloud mask and type from SAFNWC. *International Journal of Remote Sensing*, **26** (21), 4707–4732.
- Eck, T. F., B. Holben, J. Reid, O. Dubovik, A. Smirnov, N. O'neill, I. Slutsker, and S. Kinne, 1999: Wavelength dependence of the optical depth of biomass burning, urban, and desert dust aerosols. *Journal of Geophysical Research: Atmospheres*, **104**, 31 333–31 349.
- ECMWF, 2020a: *IFS Documentation CY47R1 - Part IV: Physical Processes*. IFS Documentation, ECMWF, <https://doi.org/10.21957/cpmkqvija>.
- ECMWF, 2020b: *IFS Documentation CY47R1 - Part V: Ensemble Prediction System*. IFS Documentation, ECMWF, <https://doi.org/10.21957/d7e3hrb>.
- ECMWF, 2021a: *IFS Documentation CY47R3 - Part IV: Physical Processes*. IFS Documentation, ECMWF, <https://doi.org/10.21957/eyrpir4vj>.
- ECMWF, 2021b: Operational configurations of the ECMWF integrated forecasting system (IFS). Web page. URL <https://www.ecmwf.int/en/forecasts/documentation-and-support>, accessed: 2021-012-20.
- Efron, B., and R. J. Tibshirani, 1994: *An introduction to the bootstrap*. CRC press.
- Escudero, M., and Coauthors, 2005: Wet and dry african dust episodes over eastern spain. *Journal of Geophysical Research: Atmospheres*, **110**.
- EUMETSAT, 2009: EUMETSAT data services - cloud mask - MSG - 0 degree. Web page. URL <https://data.eumetsat.int/product/EO:EUM:DAT:MSG:CLM>, accessed: 2021-12-22.
- EUMETSAT, 2015: MSG meteorological products extraction facility algorithm specification document - SCENES ANALYSIS. Technical report. URL <https://www.eumetsat.int/media/38993>, accessed: 2021-12-22.
- EUMETSAT, 2021a: Change log for radiation products (since 1 may 2008) - SIS. Web page. URL [https://www.cmsaf.eu/EN/Products/ChangeLogs/OperationalProducts/Radiation\\_Products\\_node.html](https://www.cmsaf.eu/EN/Products/ChangeLogs/OperationalProducts/Radiation_Products_node.html), accessed: 2021-12-22.
- EUMETSAT, 2021b: Product characteristics: Interim climate data records, ICDR SEVIRI radiation, based on SARA-2 methods, SIS - surface incoming shortwave radiation. Web page. URL [https://wui.cmsaf.eu/safira/action/viewProduktDetails?eid=21985\\_21986&fid=27](https://wui.cmsaf.eu/safira/action/viewProduktDetails?eid=21985_21986&fid=27), accessed: 2021-12-22.

- Flentje, H., I. Mattis, Z. Kipling, S. Rémy, and W. Thomas, 2021: Evaluation of ECMWF IFS-AER (CAM5) operational forecasts during cycle 41r1–46r1 with calibrated ceilometer profiles over germany. *Geoscientific Model Development*, **14** (3), 1721–1751.
- Francis, D., R. Fonseca, N. Nelli, D. Bozkurt, G. Picard, and B. Guan, 2022: Atmospheric rivers drive exceptional saharan dust transport towards europe. *Atmospheric Research*, **266**, 105 959.
- Gueymard, C. A., and D. Yang, 2020: Worldwide validation of CAM5 and MERRA-2 reanalysis aerosol optical depth products using 15 years of AERONET observations. *Atmospheric Environment*, **225**, 117 216.
- Hansen, J., M. Sato, and R. Ruedy, 1997: Radiative forcing and climate response. *Journal of Geophysical Research: Atmospheres*, **102** (D6), 6831–6864.
- Hartigan, J. A., 1975: *Clustering algorithms*. John Wiley & Sons, Inc.
- Hartigan, J. A., and M. A. Wong, 1979: Algorithm AS 136: A k-means clustering algorithm. *Journal of the royal statistical society. series c (applied statistics)*, **28** (1), 100–108.
- Haywood, J., and O. Boucher, 2000: Estimates of the direct and indirect radiative forcing due to tropospheric aerosols: A review. *Reviews of geophysics*, **38** (4), 513–543.
- Hersbach, H., and Coauthors, 2020: The ERA5 global reanalysis. *Quarterly Journal of the Royal Meteorological Society*, **146** (730), 1999–2049.
- Holben, B. N., and Coauthors, 1998: AERONET—a federated instrument network and data archive for aerosol characterization. *Remote sensing of environment*, **66** (1), 1–16.
- Holben, B. N., and Coauthors, 2001: An emerging ground-based aerosol climatology: Aerosol optical depth from AERONET. *Journal of Geophysical Research: Atmospheres*, **106**, 12 067–12 097.
- Hoshyaripour, A., 2021: February 2021: A dusty month for europe. Web page, EGU blogs. URL <https://blogs.egu.eu/divisions/as/2021/04/03/february-2021-a-dusty-month-for-europe/>, accessed: 2022-02-17.
- Isono, K., M. Komabayasi, and A. Ono, 1959: The nature and the origin of ice nuclei in the atmosphere. *Journal of the Meteorological Society of Japan. Ser. II*, **37** (6), 211–233.
- Israelevich, P., E. Ganor, P. Alpert, P. Kishcha, and A. Stupp, 2012: Predominant transport paths of saharan dust over the mediterranean sea to europe. *Journal of Geophysical Research: Atmospheres*, **117**.
- Karydis, V., P. Kumar, D. Barahona, I. Sokolik, and A. Nenes, 2011: On the effect of dust particles on global cloud condensation nuclei and cloud droplet number. *Journal of Geophysical Research: Atmospheres*, **116**.

- Knapp, K. R., and Coauthors, 2011: Globally gridded satellite observations for climate studies. *Bulletin of the American Meteorological Society*, **92** (7), 893–907.
- Köhler, C., and Coauthors, 2017: Critical weather situations for renewable energies—part b: Low stratus risk for solar power. *Renewable Energy*, **101**, 794–803.
- Ladwig, W., 2018: wrf-python (version 1.1.3)[computer software manual]. Technical report.
- Liao, H., and J. Seinfeld, 1998: Radiative forcing by mineral dust aerosols: sensitivity to key variables. *Journal of Geophysical Research: Atmospheres*, **103**, 31 637–31 645.
- Lohmann, U., and J. Feichter, 2005: Global indirect aerosol effects: a review. *Atmospheric Chemistry and Physics*, **5** (3), 715–737.
- Magnusson, Ivan Tsonevsky, Mark Parrington, Johannes Flemming, and Richard Forbes, 2021: *Saharan dust events in the spring of 2021*, Newsletter, Vol. No. 168. ECMWF, 2–3 pp.
- Meloni, D., A. Di Sarra, G. Biavati, J. DeLuisi, F. Monteleone, G. Pace, S. Piacentino, and D. Sferlazzo, 2007: Seasonal behavior of saharan dust events at the mediterranean island of lampedusa in the period 1999–2005. *Atmospheric Environment*, **41** (14), 3041–3056.
- Mielonen, T., A. Arola, M. Komppula, J. Kukkonen, J. Koskinen, G. De Leeuw, and K. Lehtinen, 2009: Comparison of CALIOP level 2 aerosol subtypes to aerosol types derived from AERONET inversion data. *Geophysical Research Letters*, **36** (18).
- Morcrette, J., A. Benedetti, A. Ghelli, J. Kaiser, and A. Tompkins, 2011: Aerosol-cloud-radiation interactions and their impact on ECMWF/MACC forecasts. Technical memorandum, ECMWF. URL <https://www.ecmwf.int/sites/default/files/elibrary/2011/11283-aerosol-cloud-radiation-interactions-and-their-impact-ecmwfmacc-forecasts.pdf>, accessed: 2021-06-20.
- Moulin, C., and Coauthors, 1998: Satellite climatology of african dust transport in the mediterranean atmosphere. *Journal of Geophysical Research: Atmospheres*, **103**, 13 137–13 144.
- Muhs, D. R., J. M. Prospero, M. C. Baddock, and T. E. Gill, 2014: Identifying sources of aeolian mineral dust: Present and past. *Mineral Dust*, Springer, 51–74.
- Mulcahy, J., D. Walters, N. Bellouin, and S. Milton, 2014: Impacts of increasing the aerosol complexity in the met office global numerical weather prediction model. *Atmospheric Chemistry and Physics*, **14** (9), 4749–4778.
- Newell, R. E., N. E. Newell, Y. Zhu, and C. Scott, 1992: Tropospheric rivers?—a pilot study. *Geophysical research letters*, **19** (24), 2401–2404.
- O’neill, N., T. Eck, A. Smirnov, B. Holben, and S. Thulasiraman, 2003: Spectral discrimination of coarse and fine mode optical depth. *Journal of Geophysical Research: Atmospheres*, **108**.

- Pfeifroth, U., and J. Trentmann, 2018: Algorithm theoretical baseline document, ICDR SEVIRI radiation based on SARA-H2 methods. Technical memorandum, ECMWF. URL [https://www.cmsaf.eu/SharedDocs/Literatur/document/2018/saf\\_cm\\_dwd\\_icdr\\_sev\\_rad\\_atbd\\_1\\_3\\_pdf.html](https://www.cmsaf.eu/SharedDocs/Literatur/document/2018/saf_cm_dwd_icdr_sev_rad_atbd_1_3_pdf.html), accessed: 2021-06-17.
- Reinert, D., and Coauthors, 2021: DWD database reference for the global and regional ICON and ICON-EPS forecasting system, v2.1.7. Technical report, Deutscher Wetterdienst. [https://doi.org/10.5676/DWD\\_pub/nwv/icon\\_2.1.7](https://doi.org/10.5676/DWD_pub/nwv/icon_2.1.7).
- Rieger, D., A. Steiner, V. Bachmann, P. Gasch, J. Förstner, K. Deetz, B. Vogel, and H. Vogel, 2017: Impact of the 4 april 2014 saharan dust outbreak on the photovoltaic power generation in germany. *Atmospheric Chemistry and Physics*, **17** (21), 13 391–13 415.
- Rieger, D., and Coauthors, 2015: ICON–ART 1.0—a new online-coupled model system from the global to regional scale. *Geoscientific Model Development*, **8** (6), 1659–1676.
- Rodriguez, S., X. Querol, A. Alastuey, G. Kallos, and O. Kakaliagou, 2001: Saharan dust contributions to PM10 and TSP levels in southern and eastern spain. *Atmospheric Environment*, **35** (14), 2433–2447.
- Rosenfeld, D., 2000: Suppression of rain and snow by urban and industrial air pollution. *Science*, **287** (5459), 1793–1796.
- Rémy, S., and Coauthors, 2019: Description and evaluation of the tropospheric aerosol scheme in the european centre for medium-range weather forecasts (ECMWF) integrated forecasting system (IFS-AER, cycle 45r1). *Geoscientific Model Development*, **12** (11), 4627–4659.
- Sassen, K., P. J. DeMott, J. M. Prospero, and M. R. Poellot, 2003: Saharan dust storms and indirect aerosol effects on clouds: CRYSTAL-FACE results. *Geophysical Research Letters*, **30** (12).
- Schröter, J., and Coauthors, 2018: ICON-ART 2.1: a flexible tracer framework and its application for composition studies in numerical weather forecasting and climate simulations. *Geoscientific Model Development*, **11** (10), 4043–4068.
- Shao, Y., and Coauthors, 2011: Dust cycle: An emerging core theme in earth system science. *Aeolian Research*, **2** (4), 181–204.
- Textor, C., and Coauthors, 2006: Analysis and quantification of the diversities of aerosol life cycles within AeroCom. *Atmospheric Chemistry and Physics*, **6** (7), 1777–1813.
- Trenberth, K. E., and J. G. Olson, 1988: An evaluation and intercomparison of global analyses from the national meteorological center and the european centre for medium range weather forecasts. *Bulletin of the American Meteorological Society*, **69** (9), 1047–1057.
- Twomey, S., 1974: Pollution and the planetary albedo. *Atmospheric Environment (1967)*, **8** (12), 1251–1256.

- Weger, M., and Coauthors, 2018: The impact of mineral dust on cloud formation during the saharan dust event in april 2014 over europe. *Atmospheric Chemistry and Physics*, **18 (23)**, 17 545–17 572.
- Winker, D. M., M. A. Vaughan, A. Omar, Y. Hu, K. A. Powell, Z. Liu, W. H. Hunt, and S. A. Young, 2009: Overview of the CALIPSO mission and CALIOP data processing algorithms. *Journal of Atmospheric and Oceanic Technology*, **26 (11)**, 2310–2323.
- Zhang, Y., 2008: Online-coupled meteorology and chemistry models: history, current status, and outlook. *Atmospheric Chemistry and Physics*, **8 (11)**, 2895–2932.
- Zhang, Y., C. Seigneur, J. H. Seinfeld, M. Z. Jacobson, and F. S. Binkowski, 1999: Simulation of aerosol dynamics: A comparative review of algorithms used in air quality models. *Aerosol Science & Technology*, **31 (6)**, 487–514.
- Zängl, G., D. Reinert, P. Rípodas, and M. Baldauf, 2015: The ICON (ICOsahedral non-hydrostatic) modelling framework of DWD and MPI-m: Description of the non-hydrostatic dynamical core. *Quarterly Journal of the Royal Meteorological Society*, **141 (687)**, 563–579.

# Acknowledgments

First of all I would like to express my deepest gratitude to my technical supervisors Dr. Ali Hoshyaripour and Dr. Julian Quinting. Thank you Ali, Thank you Julian for the excellent supervision and flexibility during our countless meetings throughout all phases of this project. It was very exciting working on this topic, connecting the research fields of the two working groups *Aerosols, Trace Gases and Climate Processes* and *Large-scale Dynamics and Predictability*. Your feedback from your particular fields of expertise was a great help for conducting this research. Despite the additional challenge of the pandemic situation, it was also a great personal pleasure to work with you, and your passion for atmospheric science was a great motivation for me to continue into the direction of research.

Likewise, I am very grateful to my supervisor Jun.-Prof. Dr. Christian Grams. Christian, thank you for all your valuable ideas and suggestions for further development of this project. Your feedback was a great help for structuring my research focus during the recent year. Last but not least, thank you for all advise about continuing in academia.

I also want to thank my co-supervisor Prof. Dr. Corinna Hoose for her valuable questions especially during the concept development phase of this research project. Equally I want to thank all members of the working group *Aerosols, Trace Gases and Climate Processes* for their valuable feedback, especially about my talks in the IMK-TRO seminar.

Furthermore I want to thank the supervisors of my assistant jobs, Dr. Andreas Wieser at IMK-TRO, and Constanze Kreutzer formerly at the International Office at KIT, for their great support, flexibility and exciting tasks beyond my main research project.

Finally I want to thank my friends and family all around the planet for being the amazing people I was and am gifted to experience in life. You make working on global issues especially exciting, and I highly appreciate all the extra discussions, adventures, insights you bring into my life. Beyond that, I especially want to thank my flatmates Niklas, Rebecca, Veronica for their amazing support and love!



# Erklärung

Ich versichere wahrheitsgemäß, die Arbeit selbstständig angefertigt, alle benutzten Hilfsmittel vollständig und genau angegeben und alles kenntlich gemacht zu haben, was aus Arbeiten anderer unverändert oder mit Abänderungen entnommen wurde.

Karlsruhe, den 22.02.2022

(Kilian Franz Hermes)